Summer 2024

Enhancing the Bandwidth and Radiation Characteristics of Size-Reduced Antennas

Jack P. Nemec

ENHANCING THE BANDWIDTH AND RADIATION CHARACTERISTICS OF SIZE-REDUCED ANTENNAS

by

JACK P. NEMEC

(Under the Direction of Professor Sungkyun Lim)

ABSTRACT

Electrically small antennas are researched heavily throughout electromagnetic literature due to their practicality. Antennas need to be able to fit into small places such as cell phones. However, the reduction of antenna size comes at a cost in decreasing the impedance bandwidth and radiation efficiency of the antenna. This research aims to find solutions to having sized-reduced antennas while enhancing both the impedance bandwidth and radiation characteristics of the antenna. First, the size reduction of a dual-element dipole is analyzed. Dual-element dipoles are known to have impedance bandwidth enhancing properties along with the ability to have different radiation modes. Next, this idea will be improved upon by implementing the planar version of that wire antenna to further enhance the impedance bandwidth. Planar antennas are also more practical as they can be incorporated into printed circuit boards. Finally, a tuning method to combine the first harmonic frequency with the resonant frequency is given to create a sized-reduced wideband dipole antenna. All antenna designs have experimental validation backed by simulated results.

INDEX WORDS: Electrically small antennas, dual-element antennas, planar antennas, wideband antennas, impedance bandwidth enhancement, pattern reconfigurable, harmonic resonance.

ENHANCING THE BANDWIDTH AND RADIATION CHARACTERISTICS OF SIZE-REDUCED ANTENNAS

by

JACK P. NEMEC

B.S., Georgia Southern University, 2023

M.S., Georgia Southern University, 2024

A Thesis Submitted to the Graduate Faculty of Georgia Southern University

in Partial Fulfillment of the Requirements for the Degree

MASTER OF SCIENCE IN ELECTRICAL ENGINEERING

STATESBORO, GEORGIA

ENHANCING THE BANDWIDTH AND RADIATION CHARACTERISTICS OF SIZE-REDUCED ANTENNAS

by

JACK P. NEMEC

Major Professor:	Sungkyun Lim
Committee:	Rocio Alba-Flores
	Mohammad Ahad

Electronic Version Approved:

July 2024

DEDICATION

I would like to thank my mother, Talesa Nemec, and father, Mark Nemec, for all the support they have given me. My sisters, Shelby Nemec, and Abby Nemec, for always caring for me. My closest friends, Layla McGill, Nick Hackett, Hunter Lee, Leighton Thompson, and Julio Rodriguez for being shoulders to lean on and ears to listen in stressful times.

ACKNOWLEDGMENTS

I would like to thank all the professors who agreed to do research with me. Both of my committee members, Dr. Ahad and Dr. Alba, for allowing me to research while in my undergraduate degree and helping me find what path I wanted to take. Dr. Haddad, for providing fun opportunities that pushed me to learn more about the field I love. Finally, Dr. Lim, who has gone above and beyond, and pushed me to my full potential. If not for him I would not be who I am today, and I would not have the same bright future I am excited to move forward to.

I would also like to thank all my peers in research. My best friend, Nick Hackett, when together we could do anything. Also, to the graduated students from the Antennas and Wireless Propagation Lab, Grant Evans and Jalexis Vanga Guzman, for teaching, helping, and guiding me to where I am today.

TABLE OF CONTENTS

LIST OF TABLES

LIST OF FIGURES

CHAPTER 1

INTRODUCTION

1.1 Electrically Small Antennas

Electrically small antennas are generally defined as antennas that operate at a size proportionally smaller than their wavelength. While a specific standard is not given, in the literature this is usually understood as a $kr < 1$ where k is the wavenumber and r is the maximum radius of a sphere enclosing the antenna [1]. The kr of an antenna can be calculated from its wavelength given as λ. The wavelength can be calculated from the frequency of the antenna:

$$\lambda = c/f \tag{1}$$

Where c is the speed of light through a vacuum and f is the frequency. The wavenumber of the antenna can then be calculated as:

$$k = 2\pi/\lambda \tag{2}$$

The sphere that encloses the antenna and its relationship to the wavelength are investigated by Wheeler and Chu who define the physical limits of electrically small antennas [2]-[3]. An example of the kr sphere is shown in Fig. 1.1 with an example of a $\lambda/2$ dipole. The kr of the common dipole is calculated to be $\pi/2$ or roughly 1.6.

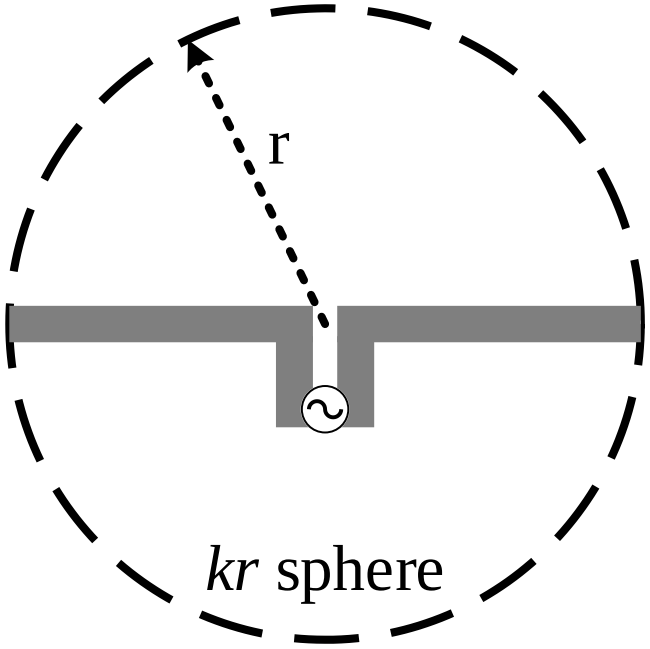

Fig. 1.1. *kr* sphere of a $\lambda/2$ dipole antenna.

Sievenpiper takes this a step further by defining the impedance bandwidth and radiation efficiency limits of electrically small antennas based on their *kr* [4]. The equation given for the bandwidth efficiency limit of electrically small antennas is given as:

$$B\eta = \frac{1}{\sqrt{2}}\left(\frac{1}{kr} + \frac{1}{(n(kr)^3)}\right)^{-1} \tag{3}$$

Where *B* is the impedance bandwidth and η is the radiation efficiency. n is represented as a 1 or 2 depending on the modes of the antenna. For example, linear polarization is a single mode and referenced as a 1. Circularly polarized antennas are dual-mode and referenced as a 2. By plotting the *kr* of an antenna versus the bandwidth efficiency $B\eta$, the physical limit of electrically small antennas is shown in Fig. 1.2, along with examples of antenna provided in [4].

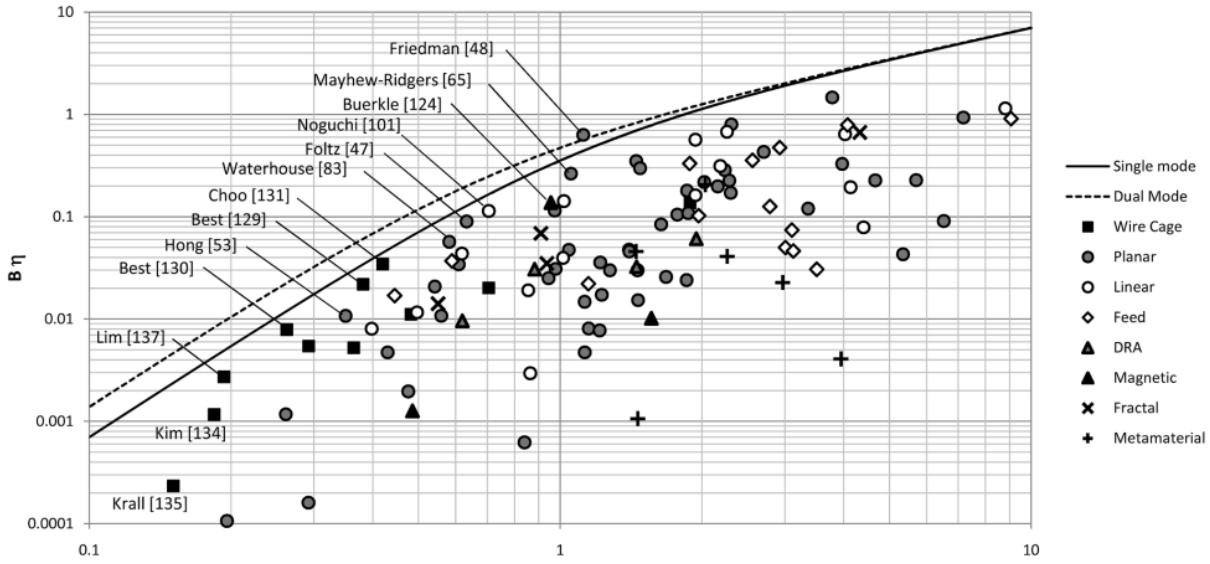

Fig. 1.2. The physical limitation of electrically small antennas [4].

It is important to note that certain antennas are not included within this limitation. Sievenpiper did not include antennas embedded in lossy materials such as water or human tissue. He also did not include ultra-wideband antennas as they usually have multi-octave bandwidths and are not considered electrically small. Of the researchers included in Fig. 1.2, many try and close the gap to be as close to the limit as possible.

To size reduce an antenna, different methods can be used such as top loading, T-matching, folding, and inductive coupling [5]-[8]. Different lossy substrates with high relative permittivity can also be used which will degrade impedance bandwidth and radiation efficiency. As this document primarily uses top loading, the other methods will not be referenced further. A simple example of top loading is given in [6], where an additional straight wire is perpendicular to the dipole element arms to decrease the frequency of the smaller antenna. To further perfect this, the T-shaped top loading can be bent into an arc that falls within the *kr* sphere to make the design as efficient as possible [5], [9]-[10]. Fig. 1.3 shows an example of how this is done. Top loading can

come in other shapes than just a T, such as a set of spirals seen in [8], or a large planar structure seen in [11].

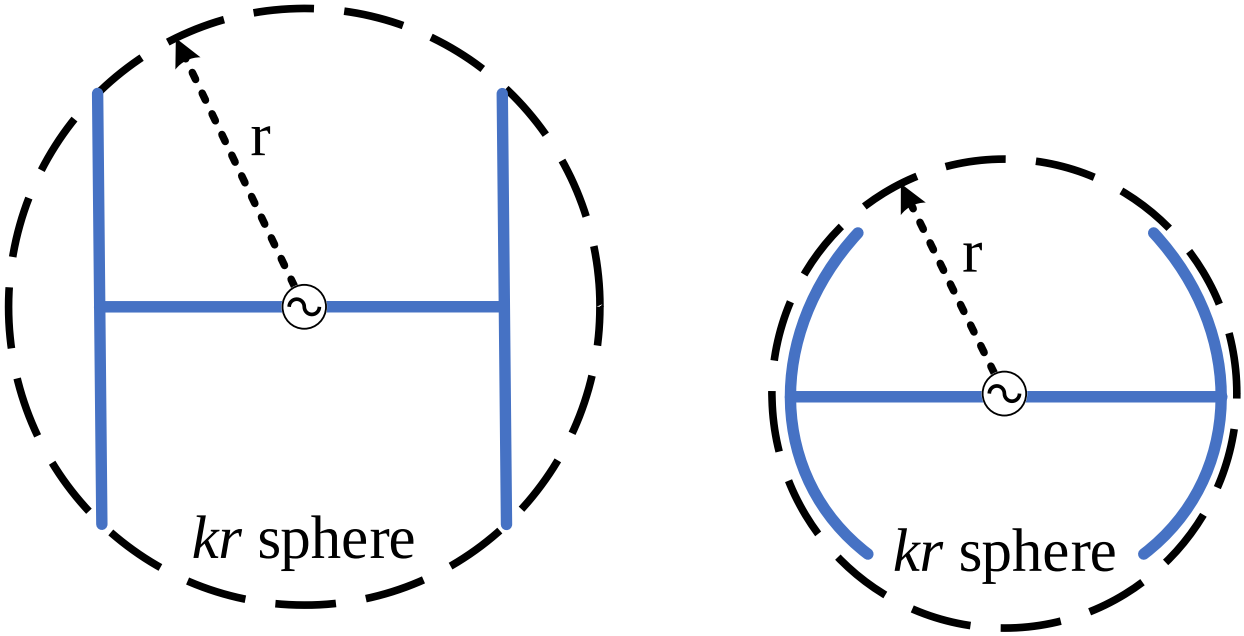

Fig. 1.3. Example of T-shape top loading within a *kr* sphere with straight wires (left) and arced wires (right).

1.2 Bandwidth Enhancements

Bandwidth enhancements can be conducted in a variety of ways. One of the most common forms is to use thick wires [9], [12]. Broadband antennas are said to have low radiation power quality, *Q*, which is defined by Wheeler and Chu [2]-[3]. Thin wire antennas have a higher *Q* than that of thick wire antennas. A strip of copper has a width equivalent to a wire with a radius of one-fourth the size [13]. In the same way thick wires are used, so can thick strips in enhancing the impedance bandwidth capabilities of an antenna [14]-[15]. Conical antennas are also known to be

more broadband. The two-dimensional version, bowtie antennas, are less broadband than conical antennas but easier to implement.

Another method of increasing the impedance bandwidth is by adding multiple antennas resonating at different frequencies onto a single feed [17]-[19]. A good example of this is log periodic dipole arrays, which combine multiple dipoles of different resonances on a single feed to obtain a very large impedance bandwidth [9], [10], [17]. Even two elements are enough to enhance the impedance bandwidth by nearly double [17], [20]-[22].

The last method related to this manuscript is using harmonics. While the $\lambda/2$ dipole is the most commonly used dipole, many more exist like the 1λ and $3\lambda/2$ dipole. These are less common as they generally have poor impedance matching or unwanted radiation characteristics but have been used to create wideband antennas [23]-[24].

1.3 Dual-Element Antennas

Dual-element antennas are a way to make wider impedance bandwidths. Another effect was analyzed in [20]-[21] where different radiation modes were observed. By adjusting the spacing between the two elements, the different modes of radiation could be tuned [20]. Fig. 1.4 shows the two radiation modes as three-dimensional realized gain patterns. The current distribution is also shown in Fig. 1.5. At the lower frequency, the current favors the longer (top) dipole more than the shorter (bottom) dipole shown in Fig. 1.5(a). Because only the longer dipole is favored, the pattern looks like a normal dipole pattern observed in Fig. 1.4(a). The same can be mentioned for the highest frequency where the current favors the shorter dipole shown in Fig. 1.4(c) and Fig. 1.5(c). At the point where the two dipoles combine, however, a change is observed in both the currents and realized gain patterns. The currents are shown to have a strong magnitude in both the longer

and shorter dipole and are nearly 180° out of phase with each other as seen in Fig. 1.5(b). This effect creates a directional mode of radiation seen in Fig. 1.4(b). The authors of [20]-[21] called both modes “dipole mode” and “Yagi mode” for the relationship to those antenna’s radiation properties. By using this antenna structure, researchers can obtain both impedance bandwidth enhancements and a frequency-dependent pattern reconfigurable antenna.

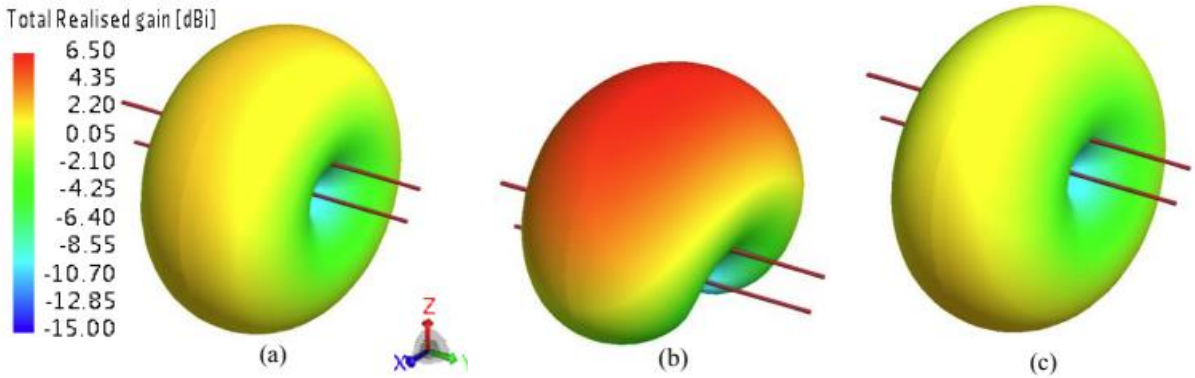

Fig. 1.4. Three-dimensional realized gain patterns of a dual-element dipole presented in [20]. (a) is the lowest frequency, (b) the center frequency, and (c) the highest frequency.

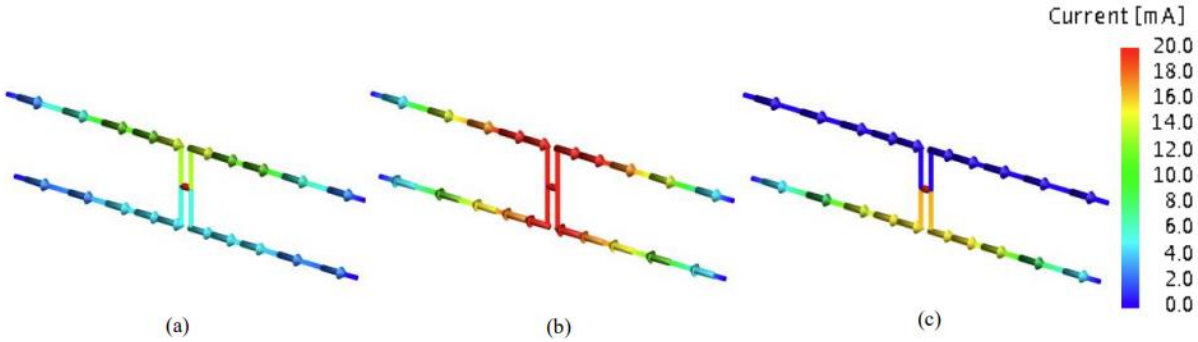

Fig. 1.5. Current distribution of the dual-element dipole presented in [21]. (a) is the lowest frequency, (b) the center frequency, and (c) the highest frequency.

1.4 Frequency Harmonics

The most common dipole is the $\lambda/2$ dipole due to its low impedance and near omnidirectional pattern, but many other types of dipoles exist. Examples of other types are the 1λ, $5\lambda/4$, $3\lambda/2$, and 2λ [12]. Each of these dipoles has different properties from the $\lambda/2$ dipole. A good way to visualize how the change in wavelength affects the currents through a dipole is shown in Fig. 1.6. Generally, 2λ dipoles are rarely used. The $3\lambda/2$ dipole can be used but the pattern is split into six separate lobes due to the change in current direction making it less practical. The $5\lambda/4$ dipole is stated to have the highest gain. In research, these different configurations can be used to create dual-band, tri-band, and even broadband antennas using one dipole structure [23]-[27]. However, in the case of utilizing the $3\lambda/2$ dipole, the patterns need to be altered to remove the grating lobes.

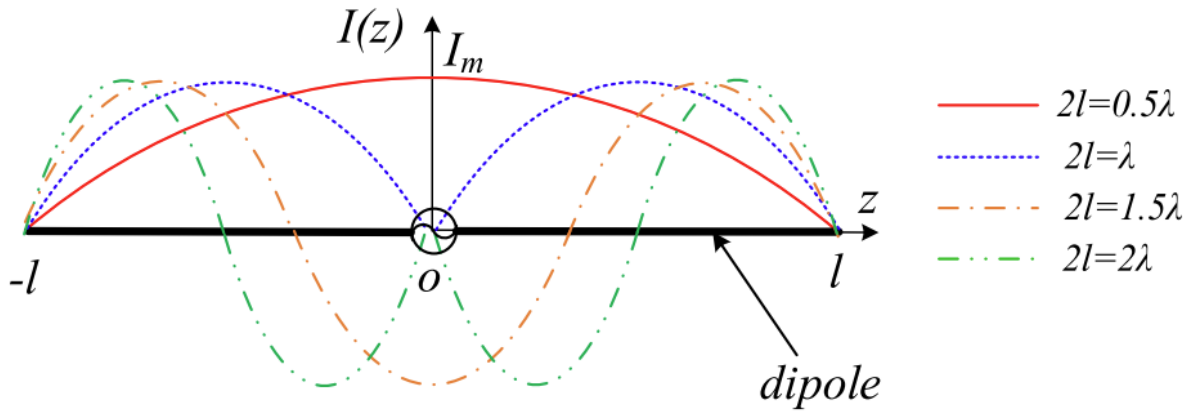

Fig. 1.6. Current distribution of different wavelength dipoles [24].

1.5 Antenna Measurement

To validate the simulation data each antenna in this manuscript will be fabricated and measured. All materials used in fabrication will be 18 AWG copper wire, FR-4 substrates with

copper traces, and lead solder. Once the antenna is fabricated it will be measured using an Agilent E5063A network analyzer. The network analyzer can measure the scattering parameters to receive the S_{11} of the antenna under test (AUT) and the S_{21} between the AUT and the measuring antenna. To ensure no outside noise or reflections cause interference with the measurements, an anechoic chamber is used shown in Fig. 1.7. It is designed to operate between 1 and 40 GHz. The carbon foam pyramids absorb electromagnetic radiation to ensure all reflections are minimized. The chamber is lined with aluminum that is grounded to prevent any outside interference from entering the chamber.

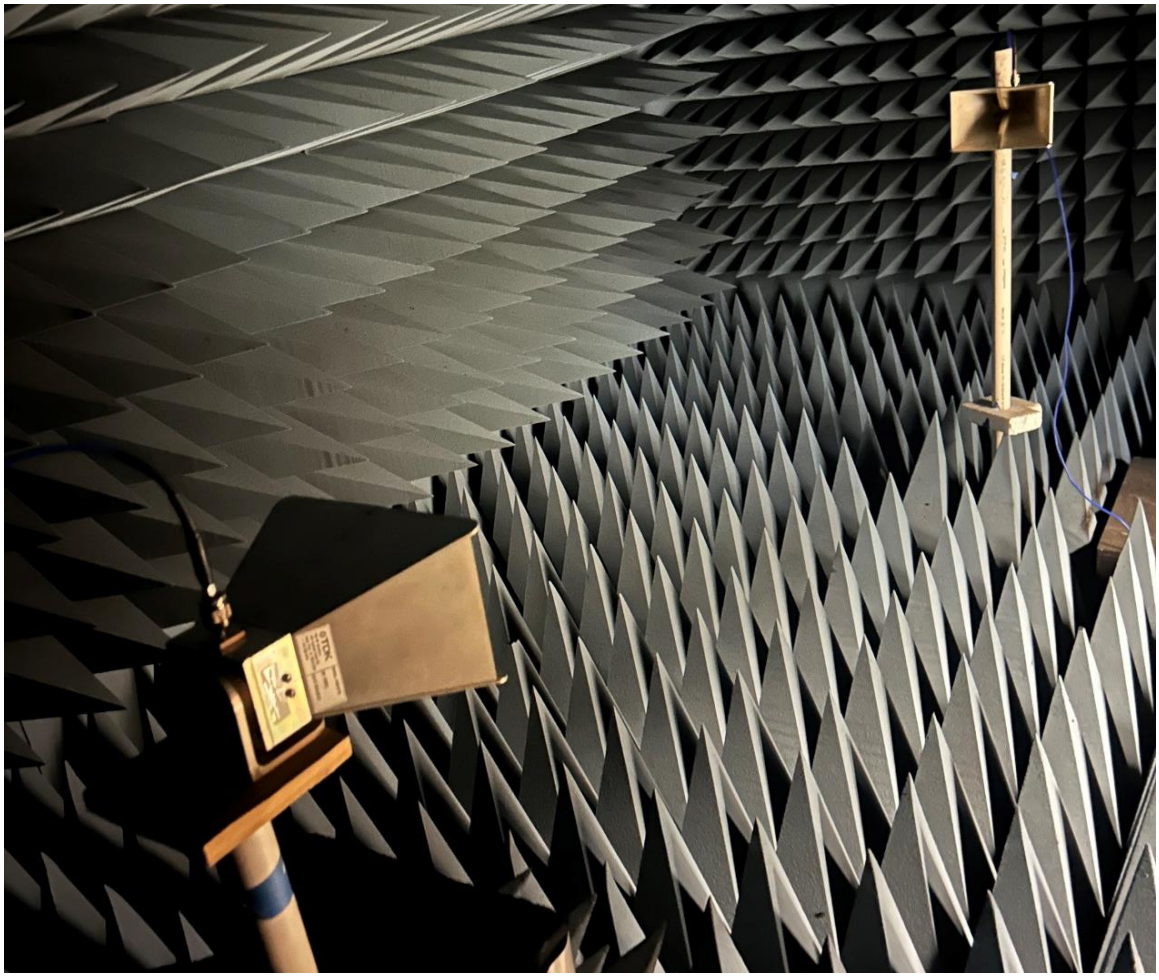

Fig. 1.7. Anechoic chamber and TDK horns used in measurement.

For a linear polarized antenna, the main measurements taken will be the S_{11}, realized gain, and the radiation patterns. The S_{11} describes the power reflected from port 1 to port 1. If the antenna is radiating properly, the reflections back to the source should be minimized. The realized gain measures how strong the radiation of an antenna is in a specific direction. To measure this the chamber needs to be calibrated with two known antennas. TDK horns, shown in Fig. 1.7, are used to get the path loss characteristics of the chamber with two antennas of a known realized gain ($|S_{21}^{H}|$). Once this value is known, the following equation can be used to calculate the realized gain of the antenna:

$$RG_{AUT} = RG_H + |S_{21}^{AUT}| - |S_{21}^{H}| \quad (4)$$

Where RG_{AUT} (dBi) is the realized gain of the AUT, RG_H (dBi) is the known realized gain of the horn antenna, $|S_{21}^{AUT}|$ (dB) is the measured S_{21} of the AUT and measuring antenna, and $|S_{21}^{H}|$ (dB) is the S_{21} of the two known horn antennas. To obtain a radiation pattern, an azimuth motor is used to rotate the antenna in a two-dimensional plane. This gives a two-dimensional cut of the radiation pattern. To get different cuts, the antenna and measuring horn can be rotated by 90°.

For dipole antennas, a balun is needed. Dipoles are a balanced antenna meaning that both arms of the dipole need to be fed by a voltage of equal magnitude but opposite phase. However, coax cables that are used to feed antennas are unbalanced. They have a voltage source on the inner conductor and a grounded shielding on the outer conductor. Balun, balanced to unbalanced, are pieces of hardware that convert unbalanced coax cables to a balanced system. For this manuscript the balun used is a Krytar model 4010265 180° hybrid balun [28], shown in Fig. 1.8, which has a very wide impedance bandwidth. The two output ports are at 0° and 180°. The two input ports are the input coax line and a 50Ω terminating resistor. Monopole antennas are unbalanced and do not require a balun making implementation easier.

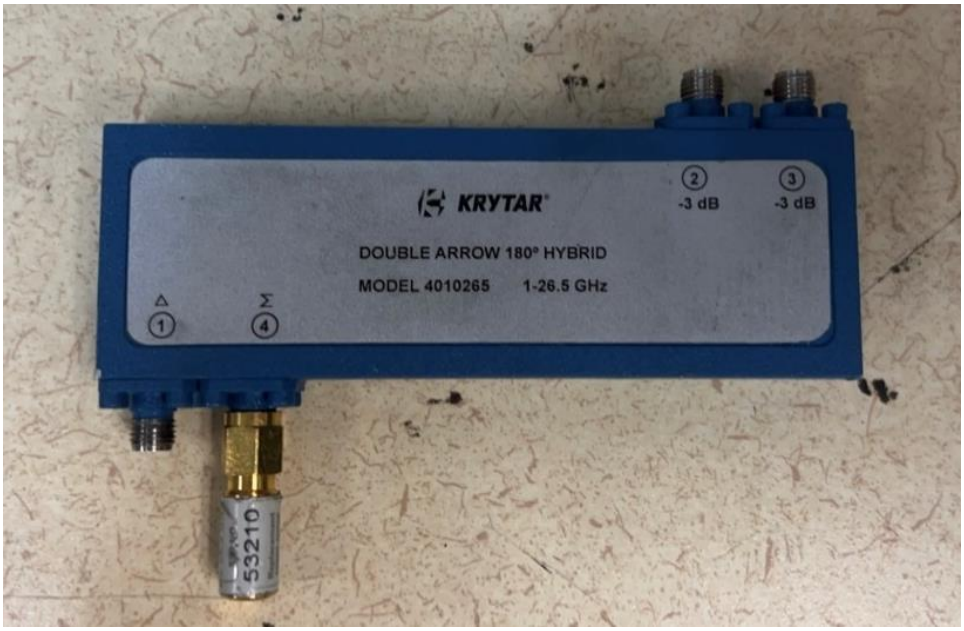

Fig. 1.8. Krytar model 4010265 180° hybrid balun.

1.6 Thesis Objective

Electrically small antennas are always defined by their impedance bandwidth and radiation efficiency limits. Many researchers push these limits as best they can to create smaller antennas with the best performance. Dual-element antennas are shown to have enhanced impedance bandwidths and now frequency-dependent pattern reconfigurable modes. In dipole antennas, the different frequency harmonics are shown to be useful in making broadband antennas although the radiation characteristics need improvement. The goal of this research is to utilize both these methods in creating size-reduced antennas while enhancing their impedance bandwidth and radiation capabilities.

First, a wire antenna version of the dual-element dipole is sized-reduced using top loading and investigated to find the smallest size with the best impedance bandwidth and radiation efficiency performance. Next, a planar dual-element monopole is investigated to show that the

dual-element antenna radiation modes can be applied to a planar setting. The antenna is reduced in size to be electrically small, and because it only contains copper traces on a single substrate, it can be easily incorporated into a printed circuit board. Finally, a method of tuning the frequency of the first harmonic of a dipole is investigated to create a wideband antenna. The antenna is then reduced in size while maintaining the wide impedance bandwidth. All antennas will be fabricated for experimental validation to back the simulated data.

CHAPTER 2

SIZE REDUCTION AND ELEMENTAL SPACING ANALYSIS OF AN ELECTRICALLY SMALL DUAL-ELEMENT DIPOLE

2.1 Abstract

An electrically small dual-element dipole is proposed. The size reduction is achieved using T-shaped top loading in a circular arc. An analysis is conducted comparing different sizes of the dual-element dipole and spacings between dipole elements to realize a better impedance bandwidth and realized gain. An antenna is realized with a *kr* of 0.9 and a spacing of 0.05λ at the frequency of the highest realized gain. The antenna shows a -10-dB impedance bandwidth of 14.86% and a peak realized gain of 6.54 dBi in the (+z) direction. The antenna shows that it contains two modes of omnidirectional "dipole mode" and directional "Yagi mode" radiation. The front-to-back ratio in Yagi mode is 19.4 dB.

2.2 Introduction

Electrically small antennas are very important for modern-day communications due to their application in many wireless technologies. However, electrically small antennas have many limitations such as reduced impedance bandwidth and radiation efficiency [2]-[4]. Studies have been conducted to improve these limitations so that electrically small antennas perform like their full-sized counterparts [5], [9]-[10]. However, these rely on parasitic elements to improve the impedance bandwidth of the antenna.

The size reduction of an antenna without the use of parasitic elements can be challenging while maintaining a large impedance bandwidth and directive radiation. Recently Huygens dipole antennas have received a lot of attention. They use near-field parasitic elements to improve their

performance while maintaining their small electrical size [29]-[31]. Huygens dipole antennas are known for having directive patterns characterized by high front-to-back ratios while maintaining their small size. However, to prioritize this the impedance bandwidth is greatly reduced. Q. Lin et al present a Huygens dipole with a large front-to-back ratio of 26.7 dB and a small impedance bandwidth of 6.3% [29]. S. -H. Lee et al present a Huygens dipole antenna with a much smaller size of 0.47 *kr* and a resulting even smaller impedance bandwidth of 1.65% [30]. While the directivity of this design is 4.66 dBi the low efficiency caused by its small size decreases the gain to 2.89 dBi.

X. Chen et al present an electrically small antenna using a meta surface as a near-field parasitic element to increase the impedance bandwidth of the antenna [32]. The design can achieve a 14.4% fractional impedance bandwidth with a near-constant dipole radiation pattern across the band. As the impedance bandwidth performance of the antenna is prioritized, the peak gain of the antenna is 1.4 dBi. Another challenge of electrically small antennas is the presence of different modes. [33]-[34] present electrically small antennas that can change their pattern characteristics or polarization by using pin diodes with multiple antennas stacked near each other. This creates complications in the design as the different states of the antenna need to be controlled with extra hardware and wiring.

Recently, a dual-element antenna design was proposed by [20]-[21]. By combining two separate resonant dipoles on a central feed and controlling the spacing, two radiation modes appear. These are coined “dipole mode” and “Yagi mode”. In dipole mode, the antenna behaves like a typical dipole. In Yagi mode, the antenna becomes directive due to alternating currents in both dipoles. This design also has an enhanced impedance bandwidth because of the two dipoles

attached to one feed. A size reduction of the antenna is presented in [22], however, the impedance bandwidth is barely larger than a half-wavelength dipole. Improvements can be made to the design.

This paper will attempt to reduce the size of this dual-element dipole to achieve an electrically small antenna with an enhanced impedance bandwidth and two modes of omnidirectional and directional patterns. The antenna will be analyzed on its size and spacing between dipole elements. Once realized, the antenna will be fabricated and measured in an anechoic chamber.

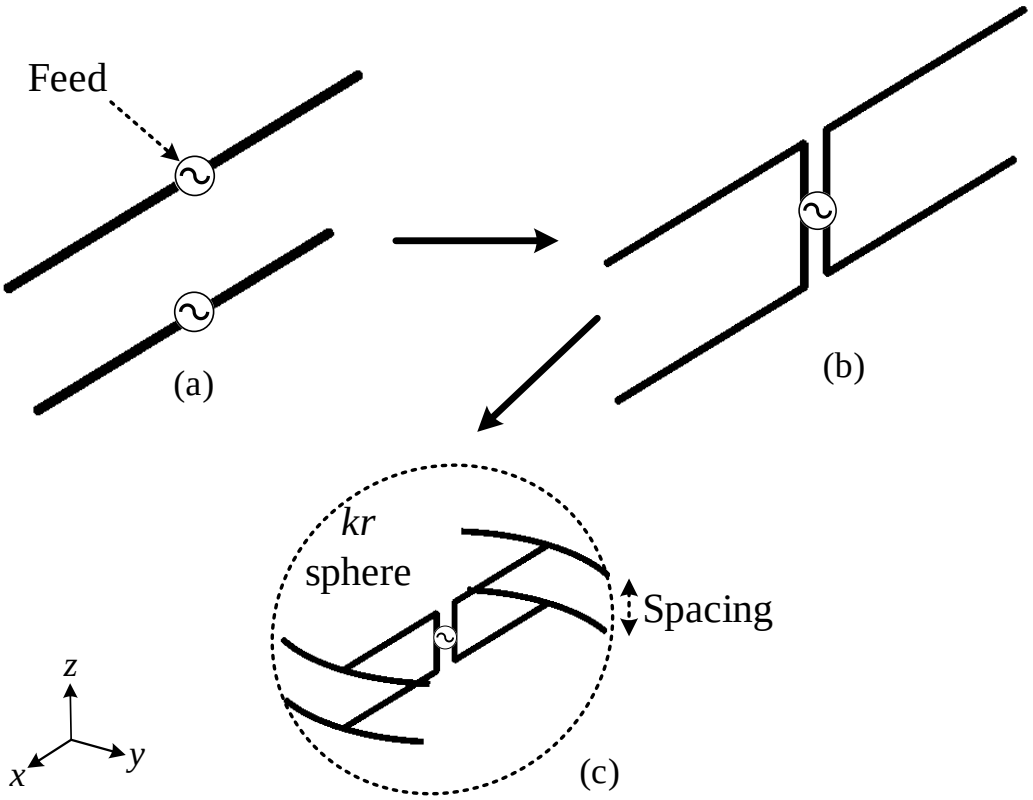

Fig. 2.1. Design procedure of an electrically small dual-element dipole.

2.3 Antenna Design Procedure

Fig. 2.1 shows the design procedure for this antenna. First, two dipoles are created at separate resonant frequencies as seen in Fig. 1(a). Next, the two dipoles are attached to a center feed shown in Fig. 2.1(b). Finally, T-shaped top loading is added to both elements to reduce the size of the individual dipoles. The top loading is arced around the radius of the *kr* sphere, seen in Fig. 2.1(c), where *k* is the wavenumber of the antenna and *r* is the maximum radius of a sphere enclosing the antenna. A methodology of comparing the size of the antenna to the spacing between the elements is conducted. To find the best size and elemental spacing of the antenna design, these aspects will be compared: impedance bandwidth, peak realized gain, and efficiency. All simulations will be conducted using Altair FEKO.

Each dual-element dipole will have a center feed connecting both dipoles. The length of each arm will be the same, however, the T-shaped top loading that arcs within the *kr* sphere will have differing lengths to differentiate the frequencies of the dipoles. Depending on both the spacing and the difference in frequency between the two dipoles, the combination point is achieved creating a moment of high directivity referred to as Yagi mode.

The analysis will be conducted by investigating different *kr* values of 0.8, 0.85, 0.9, 1.0, and 1.1. The spacing between elements will vary from 0.0375λ, 0.05λ, 0.0625λ, and 0.075λ, where λ is chosen at the combination point of 1.5 GHz. All the designs are found using a genetic algorithm optimizer where the size and space of the antenna are kept constant, and the combination point, or peak realized gain occurs at 1.5 GHz. The cost for the optimizer is given by (5) where the S_k is the S_{11} at a frequency range of 1.49 – 1.51 GHz containing 41 individual points. RG is the realized gain seen at 1.5 GHz in the $(+z)$ direction and TG is the target realized gain which was chosen to be 6.5 dBi.

$$\text{cost} = \sum_{k=1}^{41}(S_k + 10) + (TG - RG) \quad (5)$$

Fig. 2.2 shows the impedance bandwidth against the spacing of the elements. The five different lines represent the different sizes of the antenna. As expected, a kr of 0.8 proves to have the lowest impedance bandwidth ranging from 10.5 – 11.4% depending on the spacing of the two dipoles. The highest impedance bandwidth is seen by a *kr* of 1.1 ranging from 14.5 to 17.0%. A *kr* of 0.9 is shown to have a great increase from that of 0.8 and 0.85 and little difference between that of the higher sizes of 1.0 and 1.1.

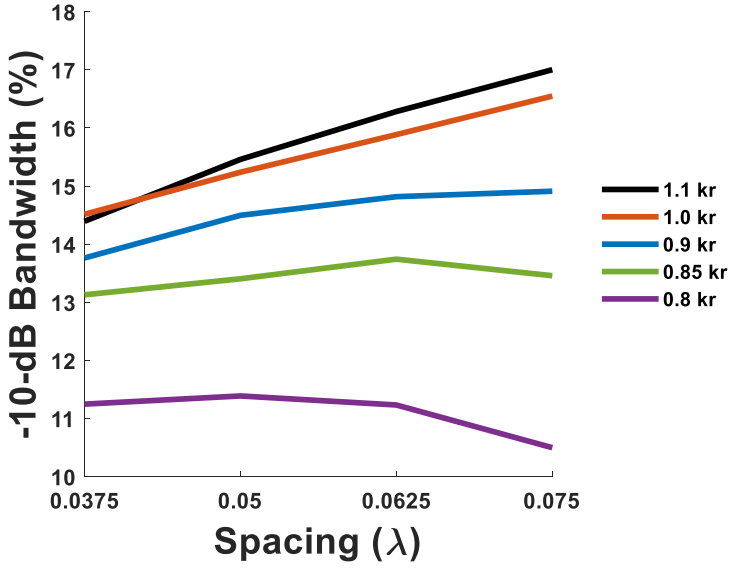

Fig. 2.2. Impedance bandwidth results for spacing and *kr* analysis.

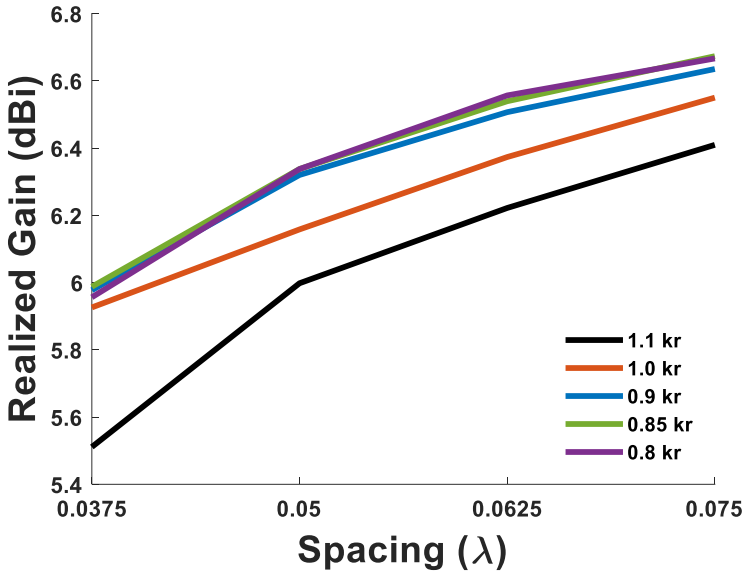

Fig. 2.3. Realized gain results for spacing and *kr* analysis.

Analyzing the realized gain in Fig. 2.3 shows that the sizes 0.8, 0.85, and 0.9 all have the highest realized gain. As the spacing increases, the realized gain also increases which is to be expected. The sizes 1.0 and 1.1 show a decreased realized gain. This can be attributed to the lower spacing chosen in this analysis. If the spacing was increased the realized gain would likely be improved but would conflict with the size reduction of the antenna.

A final analysis is done by comparing the average $B\eta$ across the different spacings, where B is the fractional impedance bandwidth and η is the radiation efficiency of the antenna at 1.5 GHz. The limit is given by [4] and can be represented by (3) where n represents the number of modes for the antenna. An n of 1 represents a singular mode and can be likened to linearly polarized antennas and an n of 2 is for dual mode antennas like a circularly polarized antenna.

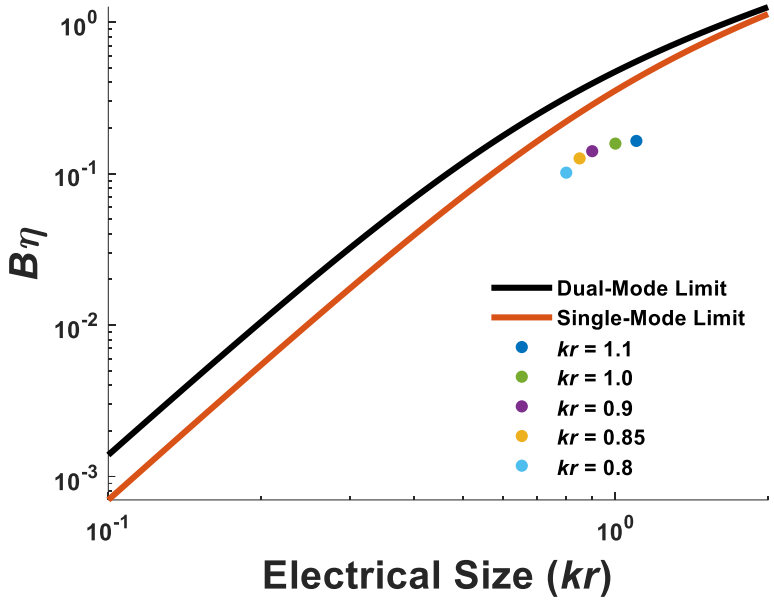

Fig. 2.4. Size-reduced dual-element dipoles compared with impedance bandwidth and radiation efficiency limit.

The results of each of the sizes averaged over the different spacing are shown in Fig. 2.4. The two sizes closest to the theoretical limit are the 0.85 and 0.9 kr antennas. Since the 0.9 kr antenna showed an improved impedance bandwidth of that over the 0.85 kr, the 0.9 kr is chosen as the size for the final design. Analyzing the spacing for both the impedance bandwidth and realized gain, there is shown to be a large jump between 0.0375λ and 0.05λ in Fig. 2.2 and Fig. 2.3. Then from 0.05λ to 0.075λ the value for the impedance bandwidth and realized gain is shown to increase slowly. While the electrical size remains the same between the different spacing, the spacing of 0.05λ is chosen as it is a lower profile but improved over the lowest spacing.

2.4 Results

The final antenna design and its dimensions are represented in Fig. 2.5. The size of the antenna is shown to be 0.9 kr with a height of 0.05λ at the frequency of peak realized gain or 1.5

GHz. The antenna is then fabricated using 18 AWG copper wire as shown in Fig. 2.5. Each element of the antenna is attached to the −3 dB ports of a Krytar, model 4005070, at 0° and 180° phase [28]. The antenna is measured using an Agilent Technologies E5063A network analyzer and an anechoic chamber.

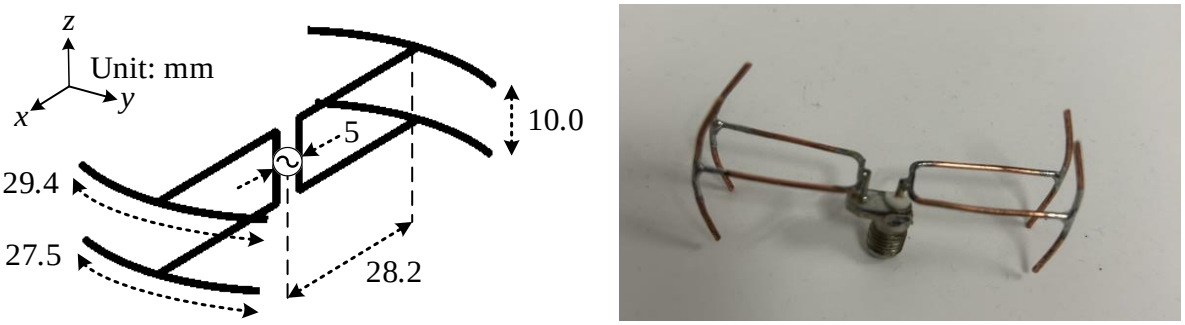

Fig. 2.5. Geometry of proposed antenna (left) and fabricated antenna (right).

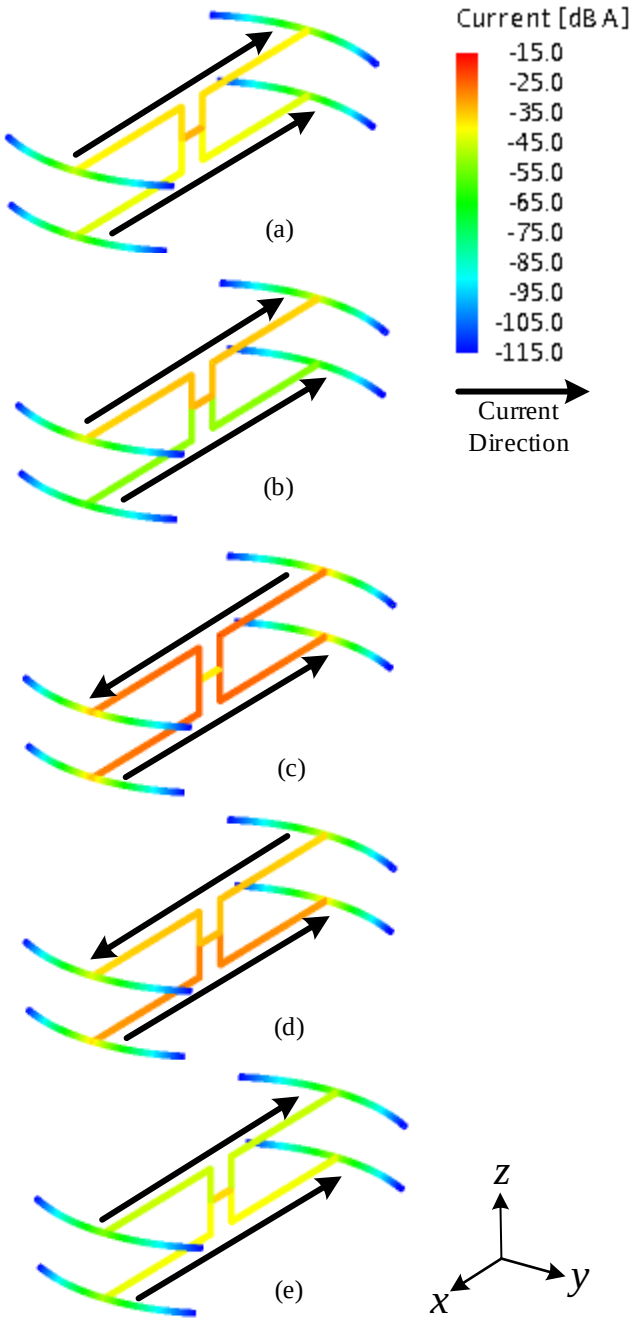

Fig. 2.6. Current distribution and directions at (a) 1.38 GHz, (b) 1.47 GHz, (c) 1.50 GHz, (d) 1.51 GHz, and (e) 1.60 GHz.

The simulated current distribution of the final design is shown in Fig. 2.6. At 1.38 GHz, the currents of both dipoles are in the same direction. However, the current in the top dipole, or

longer dipole, is shown to have a higher magnitude shown in Fig. 2.6(a). At 1.47 GHz, the antenna behaves similarly as seen in Fig. 2.6(b). At 1.50 GHz, the Yagi mode of the antenna occurs and both elements are shown to have a high current magnitude with opposing phases seen in Fig. 2.6(c). In Fig. 2.6(d), the current is shown to be dominate in the lower dipole, or shorter dipole at 1.51 GHz. At 1.60 GHz, the antenna is shown to behave as before but with a more dominating current in the lower dipole shown in Fig. 2.6(e).

The simulated and measured -10-dB impedance bandwidth is shown in Fig. 2.7. The simulated -10-dB impedance bandwidth is from 1.38 to 1.60 GHz or 14.50%. The measured -10-dB impedance bandwidth is from 1.36 to 1.58 GHz or 14.86%. These results have good agreement although the fabricated design is shown to favor the longer dipole. Due to this the combination point is at the expected frequency, however, the lower edge of the impedance bandwidth is larger than the upper edge. This can be due to the solder used during the fabrication process.

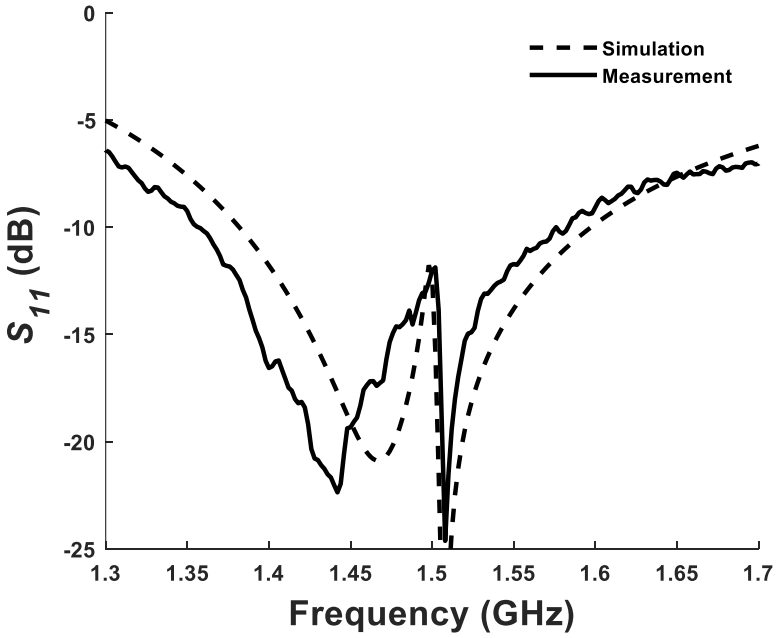

Fig. 2.7. Simulated and measured S_{11} versus frequency.

The front and back (+*z* and -*z* direction) realized gain versus frequency, in simulation and measurement shown in Fig. 2.8 also has a good agreement. The peak realized gain from Yagi mode occurs at 1.50 GHz in simulation and at 1.50 GHz in measurement. The maximum realized gain in the (+*z*) direction was simulated at 6.31 dBi and was measured to be 6.54 dBi. The minimum realized gain in the (-*z*) direction was simulated to be -9.88 dBi and was measured to be -12.86 dBi. The simulated and measured front-to-back ratio at the combination point was 16.20 and 19.40 dB respectively. In dipole mode, the front-to-back ratio is shown to be minimal in measurement. The drop in realized gain in the higher frequencies can be attributed to the frequency shift shown in the measured S_{11}.

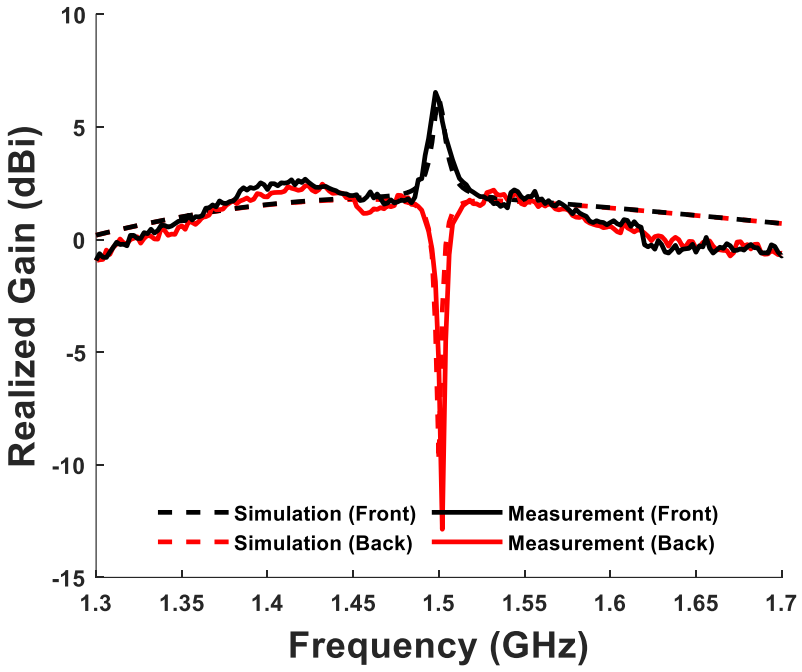

Fig. 2.8. Simulated and measured realized gain versus frequency in the (+*z*) direction and (-*z*) direction.

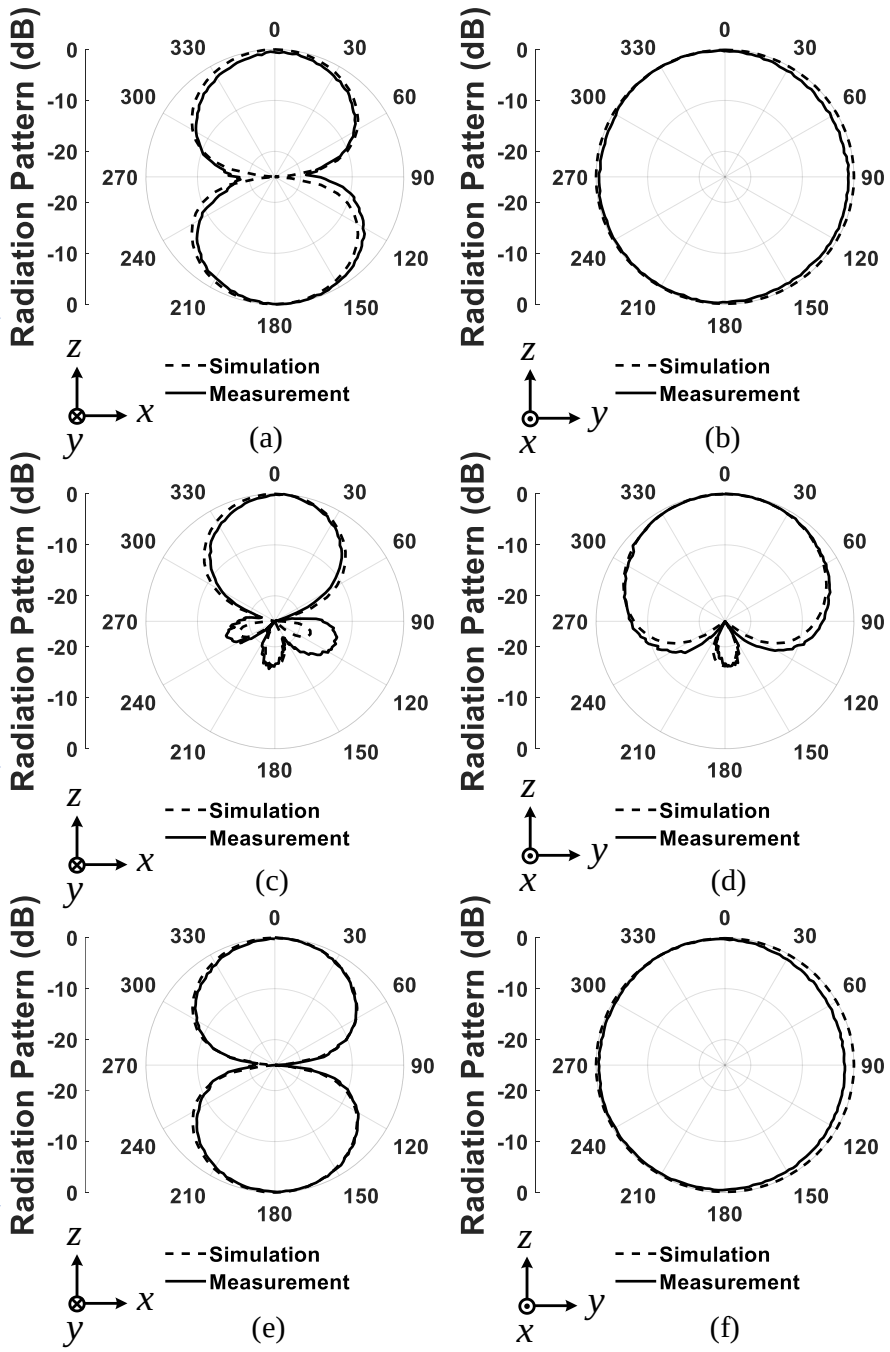

Fig. 2.9. Radiation patterns at 1.38 GHz in the XZ-plane (a) and YZ-plane (b); 1.50 GHz in the XZ-plane (c) and YZ-plane (d); and 1.60 GHz in the XZ-plane (e) and YZ-plane (f).

Three different frequencies are chosen to display the radiation patterns of the antenna. Two frequencies at the edges of the impedance bandwidth, and one at the combination point. These

values are 1.38, 1.50, and 1.60 GHz. Fig. 2.9 shows the simulated and measured radiation patterns for these frequencies in the XZ-plane and YZ-plane. The dipole mode at 1.38 GHz is shown in the XZ-plane, Fig. 2.9(a), and has nulls in the (*x*) direction which is to be expected from a conventional dipole. As seen in the YZ-plane, Fig. 2.9(b), the pattern is mostly omnidirectional. The same can be stated for 1.598 GHz, Fig. 2.9(e)(f). In Yagi mode at 1.5 GHz, the pattern is shown to be directional with a large front-to-back ratio. In the XZ-plane, Fig. 2.9(c), the simulated 3-dB beamwidth is 68° (-34°-34°) and measured 58° (-28°-30°). In the YZ-plane, Fig. 2.9(d), the simulated -3-dB beamwidth is 118° (-59°-59°) and measured 125° (-59°-66°).

Table I shows a comparison of the proposed antenna to that of other electrically small dipoles. The two main types being compared are Huygen dipoles and dipoles containing near-field radiating elements to improve both impedance bandwidth and efficiency. From the table, it is shown that the proposed antenna has the highest impedance bandwidth (IBW) and the second lowest *kr*. It only compares to one other antenna from having both omnidirectional (OD) and directional (DR) patterns. The proposed antenna also has the highest realized gain (RG) compared with other electrically small antennas of similar sizes.

TABLE I
Comparison of Electrically Small Dipoles

Reference	IBW (%)	*kr*	Pattern Type	Peak RG (dBi)
[29]	8.79/6.3	0.91/0.96	DR	4.7/5.6
[30]	1.65	0.47	DR	2.89 (Gain)
[31]	1.2	0.94	DR	2.33
[32]	14.4	0.987	OD	1.4
[33]	12.9	0.94	DR	4.43
[34]	1.9/1.7	0.98	OD + DR	3.22
Proposed	14.86	0.9	OD + DR	6.34

2.5 Conclusion

An electrically small dual-element dipole is presented to achieve a large impedance bandwidth and two radiation modes. A study was conducted changing different sizes of the antenna and spacing between the two dipole elements while comparing the impedance bandwidth and realized gain of the antenna. The best design was chosen with a size of 0.9 *kr* and a spacing of 0.05λ between the two elements. The measured impedance bandwidth was 14.86% (1.36 - 1.58 GHz). The antenna is shown to have dipole mode up to 1.50 GHz where Yagi mode occurs with a peak realized gain of 6.54 dBi and a front-to-back ratio of 19.40 dB. After 1.50 GHz the antenna is shown to go back to dipole mode until the edge of the impedance bandwidth. In Yagi mode, the 3dB-beamwidth is 58° (-28-30°) in the XZ-plane and 125° (-59-66°) in the YZ-plane.

CHAPTER 3

DESIGN OF AN ELECTRICALLY SMALL PLANAR DUAL-ELEMENT MONOPOLE

3.1 Abstract

An electrically small planar dual-element monopole is presented. An analysis is done on the feedline and ground plane to improve the impedance matching of the antenna while rejecting unwanted radiation characteristics. The antenna is then reduced in size, yielding a kr of 0.999 at 1.2 GHz. The antenna shows a -10-dB impedance bandwidth of 43.11% (1.185-1.836 GHz) and a peak realized gain of 2.069 dBi in the (+*x*) direction at 1.381 GHz. The antenna shows that it contains two modes of omnidirectional and directional radiation. The front-to-back ratio in the directional mode is measured to be 7.500 dB. The antenna shows improved benefits over its wire counterparts with a much larger impedance bandwidth and easier implementation and fabrication.

3.2 Introduction

Planar antennas are very important to the modern communication world. This is because they are cost effective, easy to manufacture, and are low-profile. Many wire antenna types have alternatives that can be made with planar structures [18], [35]-[40]. Among other benefits, planar designs are good because they can be incorporated into printed circuit boards unlike wire or leaky wave antennas [35]. This gives flexibility in overall system design and cost. A good example of this is in phased array architecture, where tiling planar antennas is shown to be very cost-effective [41]. Other structures like slats would cost much more as hardware is not easily implemented. In many modern devices, planar antennas are becoming the most common type.

One example of a wire structure that can be mimicked with a planar antenna is a monopole. Monopoles, commonly λ/4 wire monopoles, are one of the most common types of antennas. They

are used in widespread technologies like AM and FM radio, VHF and UHF communications, and cellular devices. The monopole can be implemented on a planar substrate using a parallel ground plane and feedline. These antennas are shown to have very wideband characteristics within the literature [18], [35]-[39]. Having a parallel ground plane allows for implementation into a printed circuit board. Another benefit of a monopole is that additional hardware such as a balun is not needed as they are unbalanced antennas.

Recently a dual-element dipole antenna was presented in [20]-[21] which has an enhanced impedance bandwidth from that of a $\lambda/2$ dipole and two distinctive radiation modes. In the lower and upper parts of the band, the radiation favors one of the different length dipoles making an omnidirectional pattern. At the center of the band, both dipole elements radiate creating a directional pattern. The size reduction of this type of antenna was accomplished in [22]. The full-size antenna has an impedance bandwidth of 20.9% and the electrically small antenna has an impedance bandwidth of 11.5%. This is expected due to the impedance bandwidth and radiation efficiency limits of electrically small antennas [2]-[4]. Using the planar monopole structure, this impedance bandwidth can be greatly increased as an electrically small antenna.

This research aims to create an electrically small planar monopole version of the dual-element dipole antenna. The planar dual-element monopole will have a parallel ground plane to help reduce the overall size of the antenna and allow easy implementation into a printed circuit board. The results will be analyzed to show that the antenna has a larger impedance bandwidth than its wire counterparts and an omnidirectional and directional radiation mode as seen in the dual-element dipole. All simulations are conducted using the Remcom XFdtd solver. The antenna will be fabricated and measured using an anechoic chamber and an Agilent E5063A network analyzer.

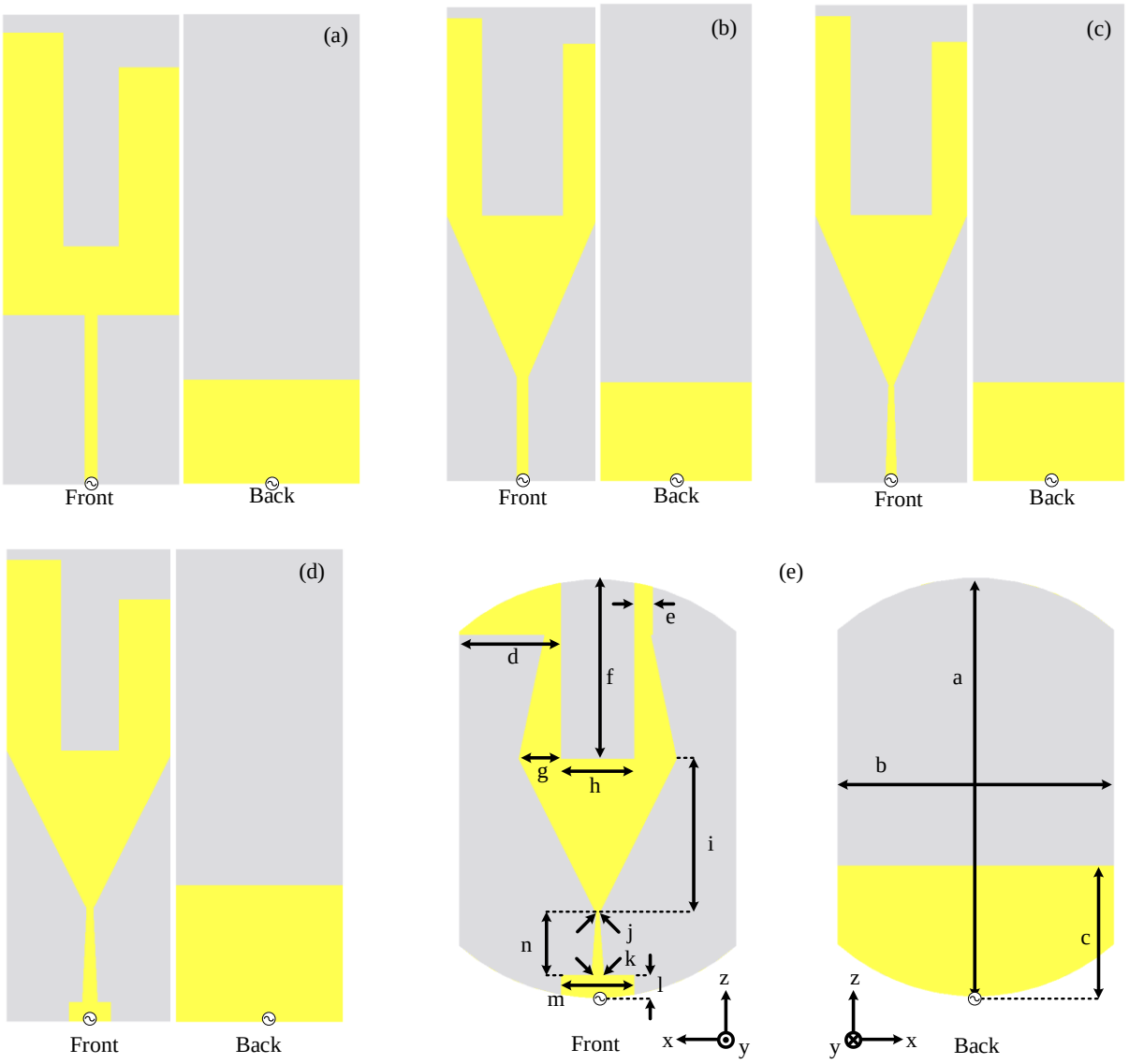

Fig. 3.1. Antenna design procedure.

3.3 Antenna Design Procedure

The design procedure for the antenna is presented in Fig. 3.1. Fig. 3.1(a) is the base of the antenna design which consists of a feedline, two elements, and a ground plane on an FR-4 substrate with 1.6 mm thickness. The feedline's length and width, along with the height of the ground plane are very important for the impedance matching of the antenna. To show the importance of these

structures, parameter sweeps are run. The length of the feedline is shown in Fig. 3.2 at 20, 30, and 40 mm. As shown, the impedance matching becomes much worse when the length is 20 or 40 mm. At 30 mm the matching is improved. Fig. 3.3 shows the effect of the feedline width at 1, 2, and 3 mm. At 1 mm, the impedance matching of the antenna worsens. At 3 mm, the impedance matching is improved in the lower edge of the frequency span. A width of 2 mm yields the highest impedance bandwidth. Fig. 3.4 has the effect of the ground plane's height at 15, 18, and 21 mm. At 15 mm, the impedance matching splits between two narrow bands. At 18 mm and 21 mm, the impedance matching is more broadband, and the latter favors the higher edge of the frequency span.

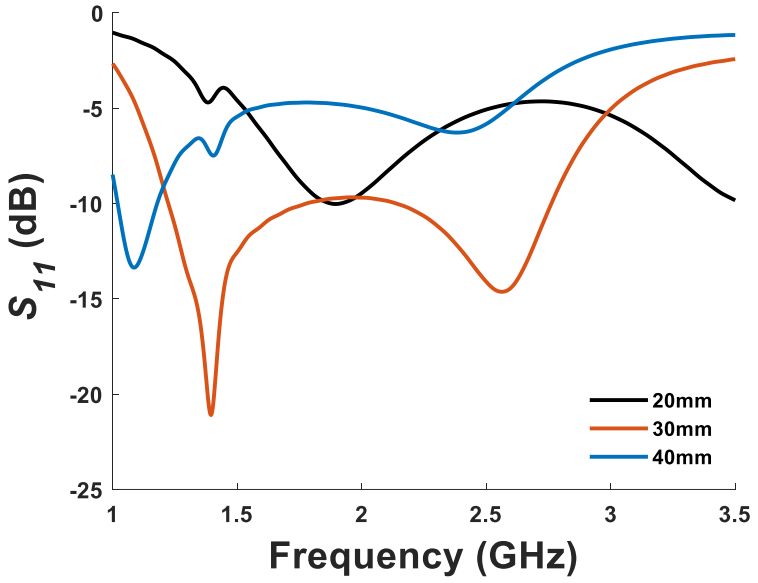

Fig. 3.2. Parameter sweep of feed line length in Fig. 3.1(a).

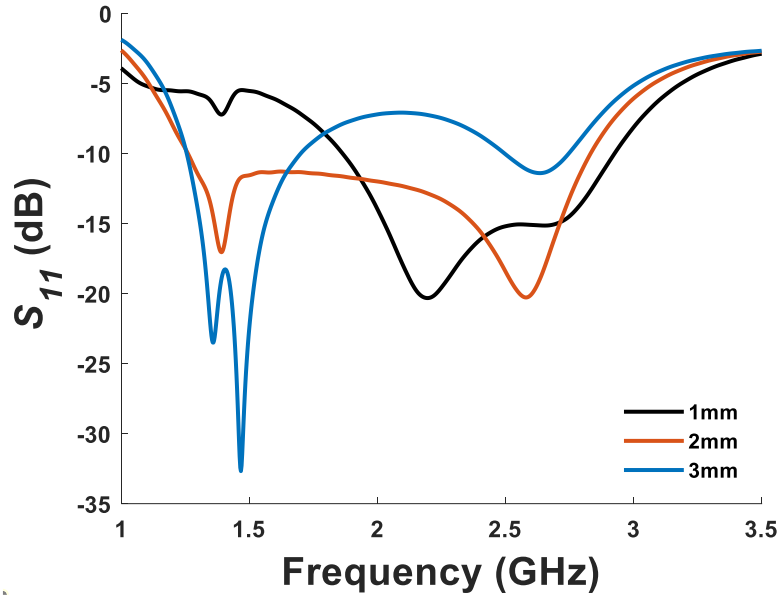

Fig. 3.3. Parameter sweep of the feed line width in Fig. 3.1(a).

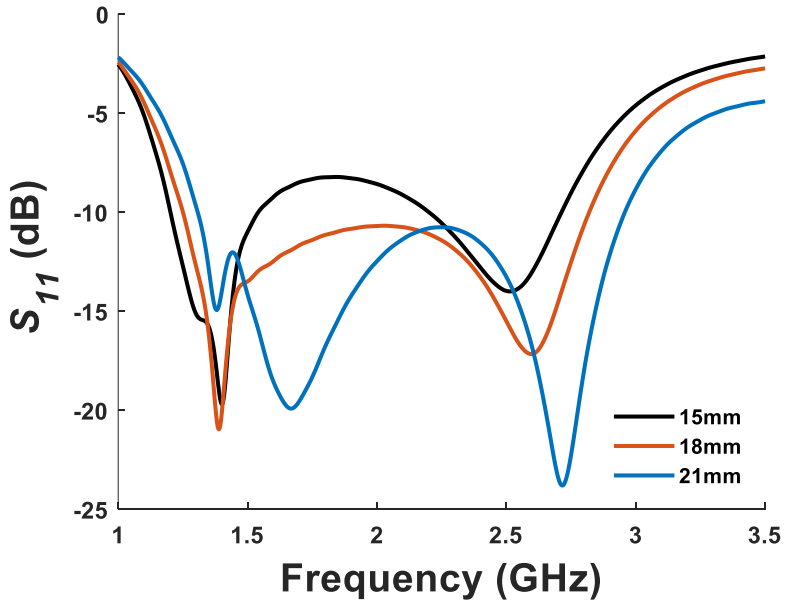

Fig. 3.4. Parameter sweep of the ground plane height in Fig. 3.1(a).

The antenna design of Fig. 1(a) is optimized using particle swarm for a large impedance bandwidth and high front-to-back ratio at the directional mode frequency. The result of the optimization is shown in Fig. 3.4. The S_{11} of this antenna is shown to be very wideband from 1.72

to 2.82 GHz or 78%. Although the lower band does not show the distinctive two dips in the impedance matching caused by the different elements, a directive mode can still be observed at 1.4 GHz shown in Fig. 3.5. The radiation patterns of this design are shown at three different frequencies in Fig. 3.5(a) in the XZ-plane and in Fig. 3.5(b) in the XY-plane. 1.24 GHz is the first edge of the frequency span and has a dipole-like omnidirectional pattern. At 1.4 GHz, the directive mode occurs, which can be seen in both planes. At 2 GHz, where the lower band transitions into the upper band, a dipole-like pattern is also shown. However, at 2.82 GHz, which is the highest frequency in the span, the pattern loses omnidirectionality in the XZ-plane. There are now two main lobes split between the (+*x*) direction and (+*z*) direction. In the (+*x*) direction, the radiation strength is nearly 5 dB less than that of the peak. Two large nulls that appear at 240° and 120° which do not appear at 1.24 and 2 GHz.

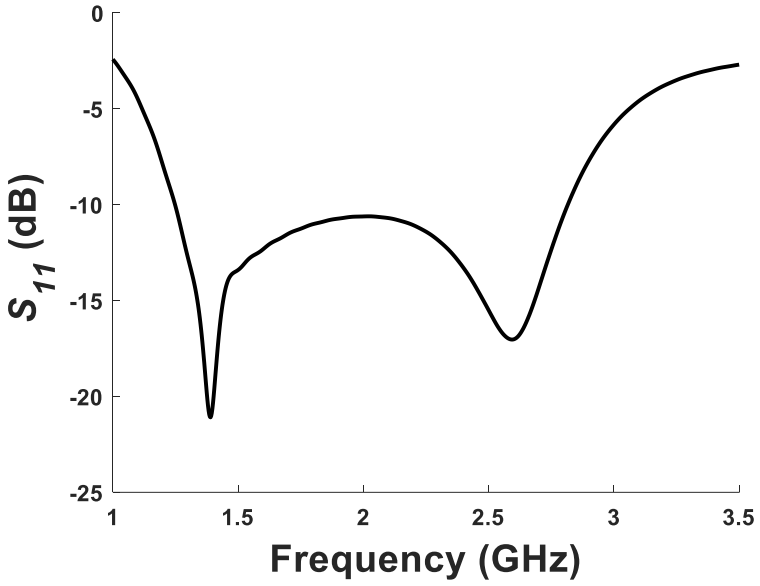

Fig. 3.5. S_{11} versus frequency of the antenna in Fig. 3.1(a).

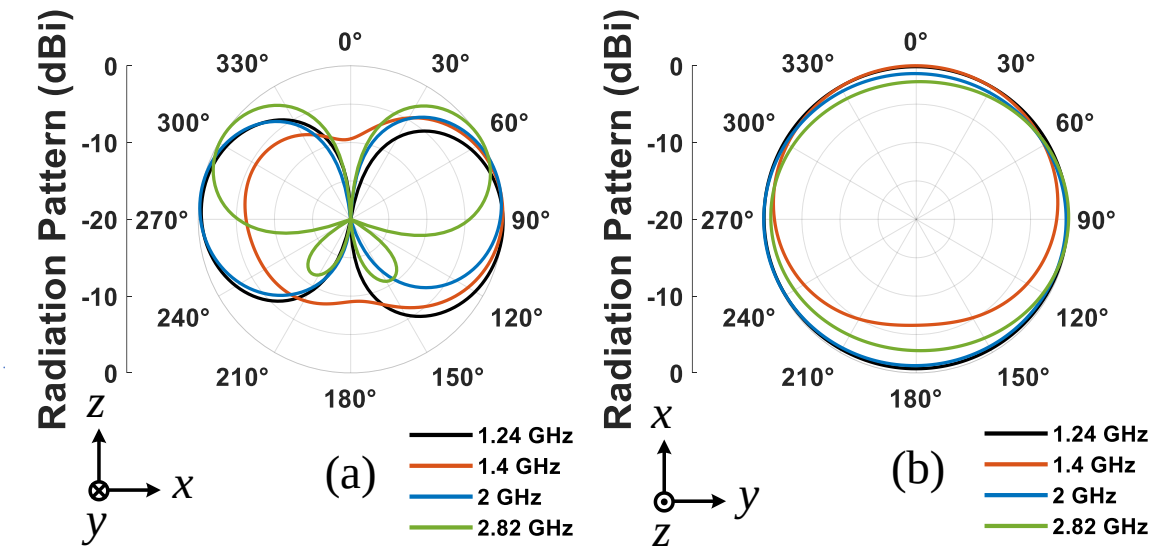

Fig. 3.6. Realized gain patterns of Fig. 1(a) in the XZ-plane (a) and XY-plane (b).

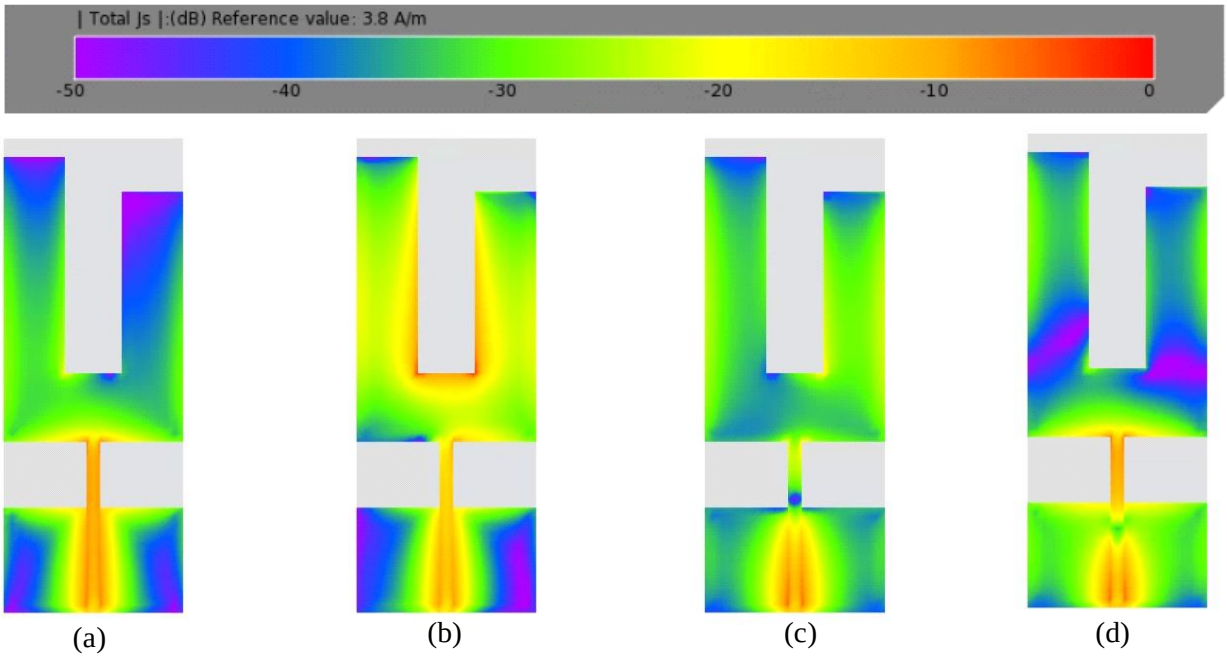

Fig. 3.7. Current distribution of Fig. 1(a) at 1.24 GHz (a), 1.4 GHz (b), 2 GHz (c), and 2.82 GHz (d).

The current distribution of this antenna at those four frequencies is shown in Fig. 3.7. At 1.24 GHz, the current is high within the feedline and favors the larger element shown in Fig. 3.7(a). This is expected with dual-element antennas. Fig. 3.7(b) shows the directional mode frequency of 1.4 GHz where the current favors both elements. Fig. 3.7(c) is at 2 GHz where the current favors the shorter element. At 2.82 GHz, the current is shown to have a null appear within the feedline shown in Fig. 3.7(d). The elements are also shown to have large nulls near their bottom edge. These nulls signify a change in the current direction and are the cause of the poor radiation pattern shown in Fig. 3.6. This is caused by a higher wavelength resonating through the antenna structure like a 3λ/2 dipole.

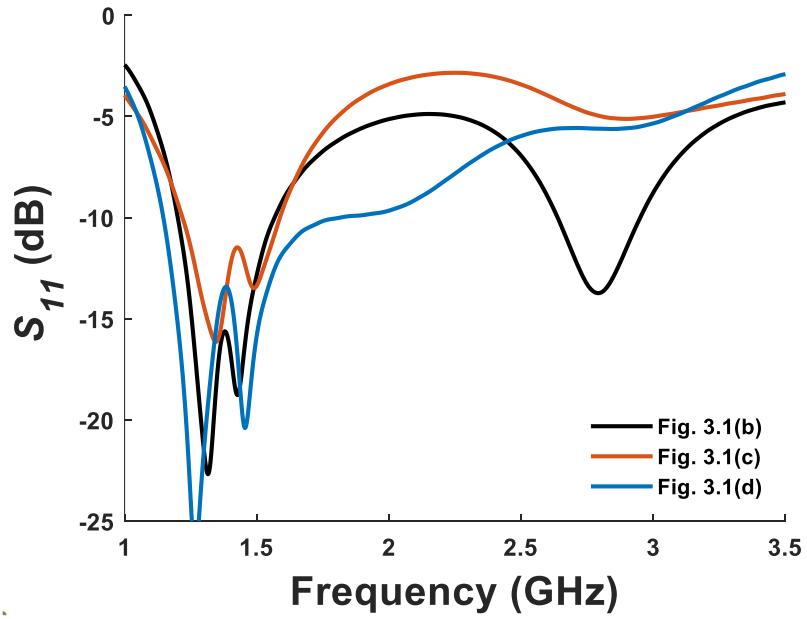

Fig. 3.8. S_{11} versus frequency of the antennas in Fig. 3.1(b)-(d).

To remove this pattern, the extra resonance will be removed altogether. Fig. 3.1(b)-(d) shows the process of how this is accomplished. Fig. 3.2-3.3 showed the importance of the feedline with the impedance matching so this is used to reject the harmonic band. Fig. 3.1(b) shows the square distribution structure being changed to a triangular one to help mitigate the resonance at

the higher frequencies. Fig. 1(c) adds a triangular feed line to fully reject the higher frequency band. Fig. 3.1(d) improved the matching of the lower frequency band and still rejects the higher frequency band. The S_{11} of these three structures is shown in Fig. 3.8. Fig. 3.1(b) is shown to help reject the higher frequency band breaking the wideband properties of Fig. 3.1(a), however, a resonance still occurs around 2.8 GHz. Fig. 3.1(c) rejects this resonance bringing the S_{11} above -5 dB. To improve the matching in the lower band to maintain more wideband characteristics, the antenna in Fig. 3.1(d) is used which is shown to have more wideband properties in the lower band.

Next, the antenna is cut into a circle of a specific radius to reduce its size. The aim is to have a *kr* of 0.999 at 1.2 GHz where *k* is the wavenumber and *r* is the maximum radius enclosing the antenna. This removal of material will shift the frequency up, so a version of top loading is added to shift it back down shown in Fig. 3.1(e). The elements are also cut into a triangular shape to increase the length along the edges of the antenna and give more room for the top-loading elements. The result of this cut is shown in Fig. 3.9. The difference between the rectangular elements and triangular elements is small in terms of impedance bandwidth. The two elements' separate resonances are better shown with the triangular elements. There is also a slight downward frequency shift observed which helps in the size reduction.

The final design structure is then optimized using a particle swarm optimizer to maximize the front-to-back ratio at the directional mode frequency and maximize the impedance bandwidth. The results of the optimization are shown in Table II which gives the dimensions to the design in Fig. 3.1(e) where λ is calculated at 1.2 GHz. With a minimum frequency of 1.2 GHz and a maximum radius of 39.75 mm, a *kr* of 0.999 is realized making the antenna electrically small. The antenna is then fabricated on an FR-4 substrate and measured using an anechoic chamber.

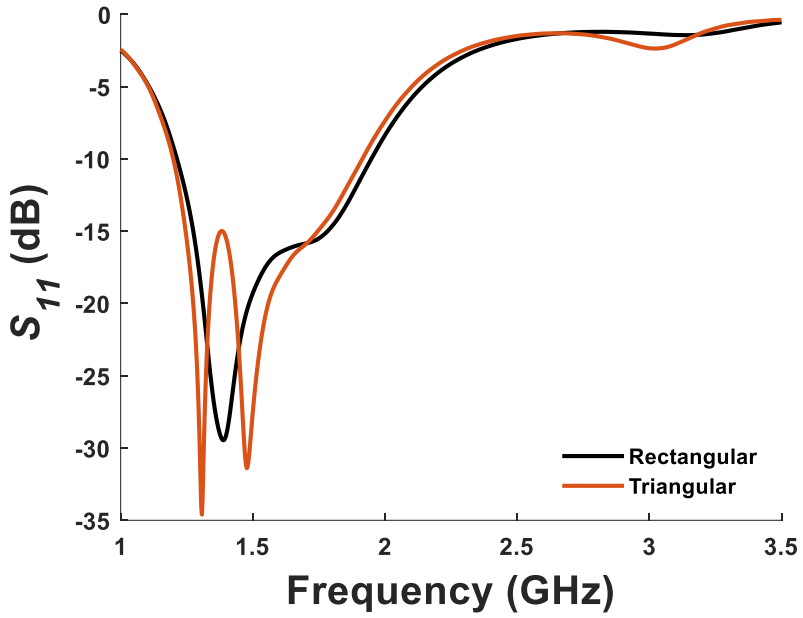

Fig. 3.9. S_{11} versus frequency of rectangular vs triangular elements.

TABLE II
Dimensions of Proposed Antenna

Desc.	mm	λ
a	79.5	0.3180
b	51.0	0.2040
c	24.8	0.0992
d	19.2	0.0768
e	3.5	0.0140
f	34.7	0.1388
g	8.0	0.0320
h	14.0	0.0560
i	29.4	0.1176
j	0.6	0.0024
k	3.1	0.0124
l	4.4	0.0176
m	13.8	0.0552
n	11.0	0.0440

3.4 Results

The fabricated antenna is shown in Fig. 3.10. The S_{11} of the antenna is shown in Fig. 3.11. The simulated -10-dB impedance bandwidth is from 1.200 to 1.913 GHz or 45.81%. The measured impedance bandwidth is 1.185 to 1.836 GHz or 43.11%. This shows good agreement between the simulated and measured results.

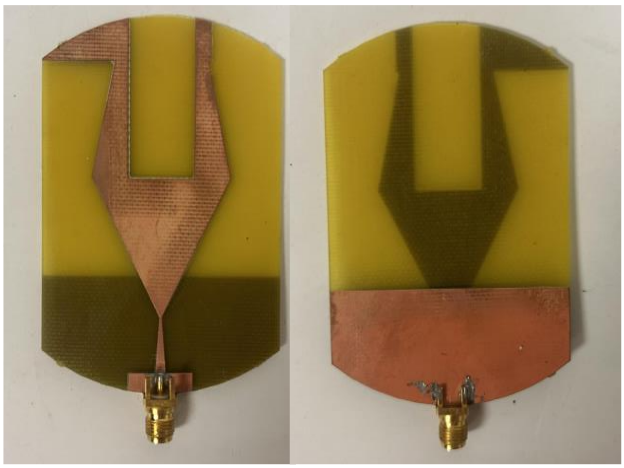

Fig. 3.10. Fabricated antenna.

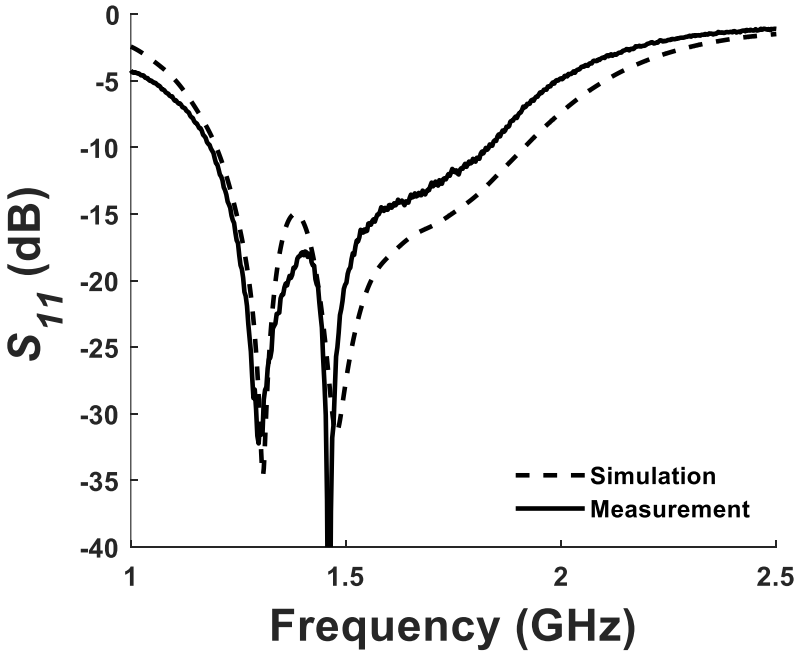

Fig. 3.11. Simulated and measured S_{11} versus frequency.

The realized gain versus frequency in the (+*x*) direction and (-*x*) direction is shown in Fig. 3.12. In simulation, the omnidirectional realized gain is around 0.6 to 1.6 dBi in the forward and backward direction. In measurement, similar realized gain values are shown. In simulation, the directional mode frequency occurs at 1.381 GHz with a peak realized gain in the (+*x*) direction of 2.113 dBi. The front-to-back ratio is calculated as 7.987 dB. In measurement, the directional mode frequency occurs at 1.381 GHz with a peak realized gain in the (+*x*) direction of 2.069 dBi. The front-to-back ratio is given as 7.500 dB. This shows good agreement between simulation and measurement.

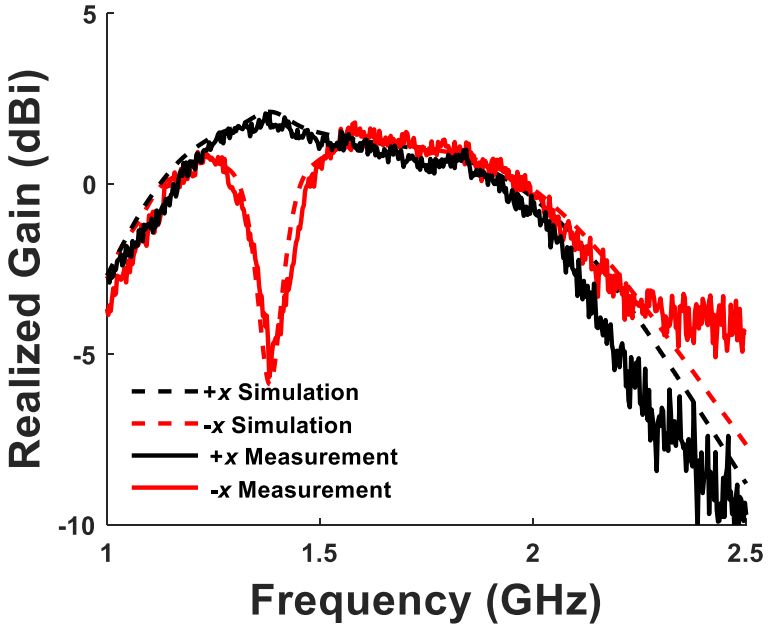

Fig. 3.12. Simulated and measured realized gain versus frequency in the (+*x*) direction and (-*x*) direction.

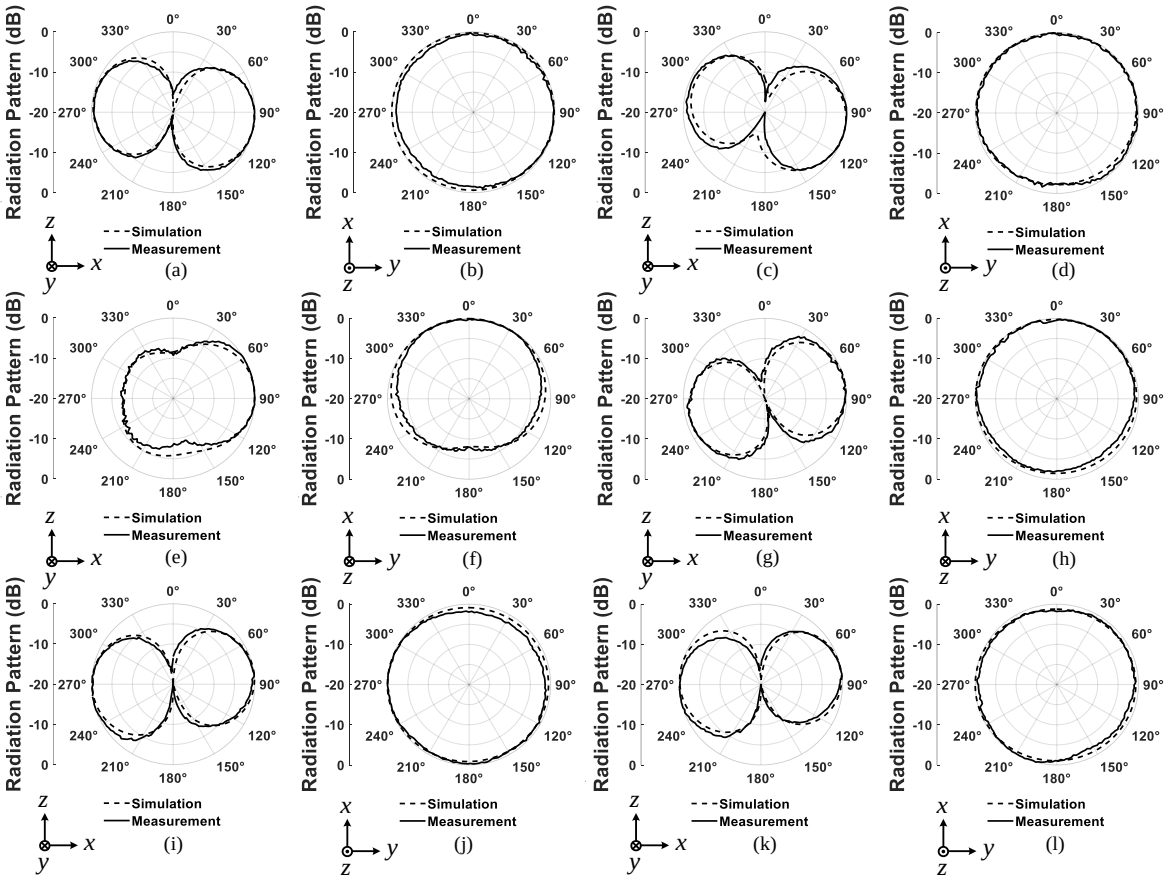

Fig. 3.13. Radiation patterns at 1.2 GHz in the XZ-plane (a) and XY-plane (b); 1.315 GHz in the XZ-plane (c) and XY-plane (d); 1.381 GHz in the XZ-plane (e) and XY-plane (f); 1.475 GHz in the XZ-plane (g) and XY-plane (h); 1.7 GHz in the XZ-plane (i) and XY-plane (j); 1.913 GHz in the XZ-plane (k) and XY-plane (l).

The radiation patterns are given in Fig. 3.13. Six frequencies are analyzed at the first frequency in the span, the frequency at the first minima in S_{11}, the directional mode frequency, the frequency at the second minima in S_{11}, a frequency between that point and the highest frequency, and the highest frequency in the span. These being 1.2, 1.315, 1.381, 1.475, 1.7, and 1.913 GHz. In the XZ-plane, the frequencies of 1.2 and 1.315 GHz, Fig. 3.13(a)(c), are shown to have a dipole-like omnidirectional pattern, however, there is a slight tilt in the patterns caused by the angle between the feed and the edge of the elements. In the XY-plane, these are also shown to be mostly

omnidirectional, Fig. 3.13(b)(d). At 1.381 GHz, the XZ-plane shows directionality in the (+*x*) direction along with the XY-plane, Fig. 3.13(e)(f). At 1.475 GHz, the pattern in the XZ-plane is dipole-like with a large tilt, Fig. 3.13(g). This occurs closer to the combination point. In the XY-plane the pattern is mostly omnidirectional, Fig. 3.13(h). At 1.7 and 1.913 GHz, the patterns in the XZ-plane are omnidirectional with a dipole-like pattern and are shown to be omnidirectional in the YZ-plane Fig. 3.13(i)-(l). The measurement results match well with that of the simulation results.

3.5 Conclusion

An electrically small planar dual-element monopole is realized with a *kr* of 0.999. In comparison with the full-size wire version presented in [20] and [21], the proposed antenna has a much higher impedance bandwidth of 43.11% compared to 20.9%. However, the radiation characteristics are not as good due to less radiation efficiency when using a substrate. In comparison with the electrically small version in [22], the impedance bandwidth of 43.11% is significantly higher than that of 11.5%.

CHAPTER 4

DESIGN OF A MINIATURIZED WIDEBAND DIPOLE UTILIZING THE FIRST FREQUENCY HARMONIC

4.1 Abstract

A miniaturized wideband dipole is proposed using a tuning method that decreases the frequency of the first frequency harmonic. The design procedure is given to show how to tune the harmonic frequency. An analysis shows that this tuning method reduces the grating lobes producing a near dipole-like pattern across the impedance bandwidth. More procedures are given for tuning the impedance of the antenna to further enhance matching. Then the antenna is cut into a circle to yield a *kr* of 1.02. The -10-dB impedance bandwidth is given as 1.17-2.546 GHz (74.06%). Through the band, the realized gain is shown to be between 1.5 and 3.0 dBi. The radiation patterns are shown to be consistent with a dipole throughout the entire impedance bandwidth in both the XZ and YZ-planes.

4.2 Introduction

Wideband antennas are good for many applications like communications, imaging, and radar [42]-[44]. The more frequencies contained within a bandwidth the more information that can be carried. Generally, antenna performance can be increased by increasing the size of the antenna, however, smaller antennas are needed with better performance. Size reduction of antennas is shown to negatively degrade both the impedance bandwidth and radiation efficiency of the antenna making small wideband antennas challenging [2]-[4].

$\lambda/2$ dipoles have another resonant frequency that occurs at three times the fundamental frequency yielding a $3\lambda/2$ dipole. This first harmonic frequency can be used as an extra band but

comes with the challenge of poor radiation characteristics. Due to the shorter wavelength propagating through the longer dipole arms, grating lobes are created. These are unwanted and make the first harmonic band less usable. Some studies have been conducted to mitigate these patterns using parasitic elements. [25] presents a slot dipole that uses the first harmonic as a second band. They add additional slots on both ends of the dipole at the edges to smoothen the grating lobes. While successful, the patterns are still inconsistent with that of a λ/2 dipole. This is expanded upon more with [26], which creates a dual-band, tri-band, and broadband application using these slots. A third example can be seen in [27]. All these antennas, while improved, do not have similar dipole-shaped patterns in the harmonic band as they do in the resonant frequency band which can be improved upon.

The harmonic resonances have also been shown to be used in other antenna designs such as [23]. The paper claims to use the first harmonic with a stagger tuning method but not much information on the method is given nor any references. The antenna design is shown to have a wide impedance bandwidth of up to 76% and omnidirectional dipole patterns. [24] presents a wideband dipole antenna over a reflector that uses both the λ/2 dipole and 1λ dipole properties. They use a branching method to achieve this and present an impedance bandwidth of 24%.

This research aims to produce a wideband antenna by tuning the first frequency harmonic that occurs at three times the fundamental frequency. The antenna will then be reduced in size to further increase its novelty. All simulations are conducted using Remcom XFdtd solver. The antenna will be fabricated and measured using an anechoic chamber and Agilent E5063A network analyzer with a Krystal 180° coupler as the balun [28].

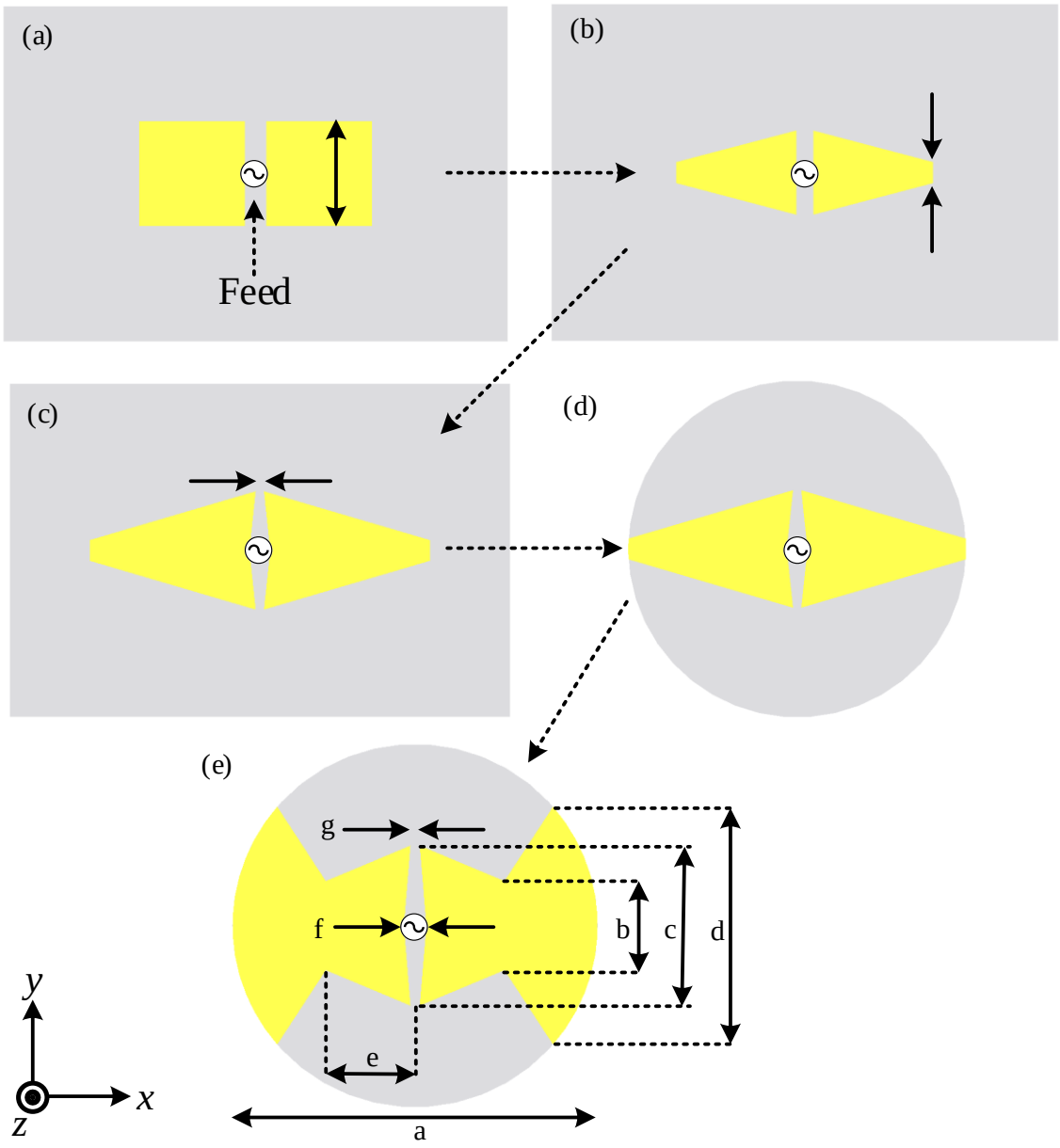

Fig. 4.1. Design procedure of the antenna.

4.3 Antenna Design Procedure

The antenna design procedure is shown in Fig. 4.1. The procedure consists of five main steps that will be discussed in this section. All antenna designs sit on top of an FR-4 substrate with a 1.6 mm thickness. The first step in Fig. 4.1(a) tunes the frequency of the first harmonic by

increasing the width of the strips. Fig. 4.1(b) shows a method for tuning impedance by changing the width of the strip away from the feed. Fig. 4.1(c) gives another method to further tune the impedance of the antenna by creating a concave shape near the feed. In Fig. 4.1(d) the antenna is cut into a sphere to reduce the overall size of the antenna. To shift the frequency down, a method of top loading is added to Fig. 4.1(e). Each of these methods is important for the performance of the antenna.

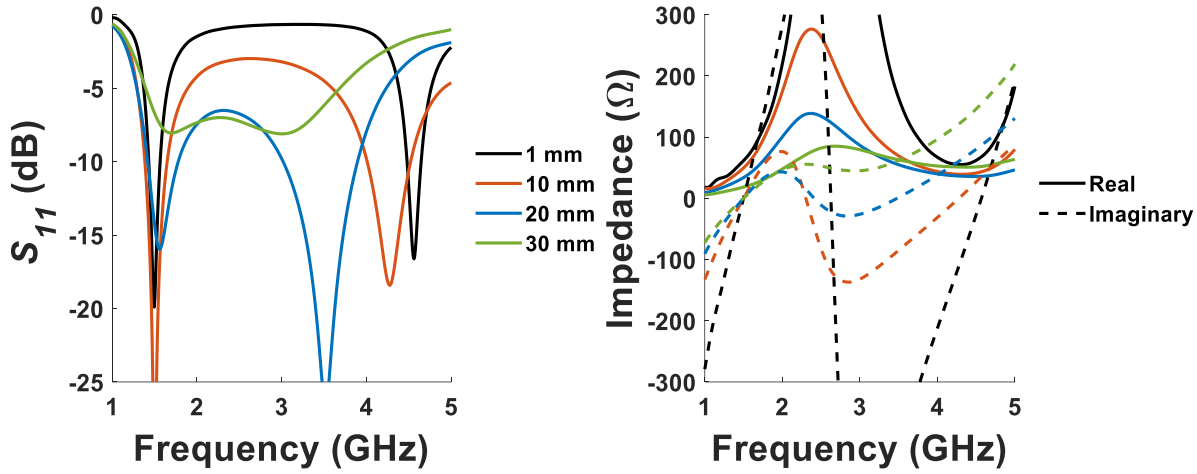

Fig. 4.2. Effect of the strip width in Fig. 4.1(a) on S_{11} (left) and input impedance (right).

By analyzing the width of the copper strips in Fig. 4.1(a), the effect of tuning the frequency of the first frequency harmonic is shown in Fig. 4.2. The dipole is tuned to have a reactance equal to 0Ω at 1.5 GHz. The widths are shown as 1 mm, 10 mm, 20 mm, and 30 mm. At a width of 1 mm, the harmonic resonance occurs at 4.5 GHz which is expected in a 3λ/2 dipole. At this frequency, the reactance reaches 0Ω for a third time. As the strip width increases, the input resistance is also shown to decrease substantially. The narrow strips have an input resistance of much greater than 300Ω in the center of the band. The dipole begins to approach 50Ω throughout the span as the strips get thicker which improves the impedance matching. There are three specific frequencies within the frequency span where the reactance is 0Ω. As the strip width increases, the

third frequency where the reactance is 0Ω is shown to decrease. This causes the frequency of the harmonic resonance to decrease. However, as the harmonic resonance begins to approach the fundamental, impedance matching worsens, due to a problem with the reactance. It begins to increase and only approaches 0Ω once at the resonant frequency. For this reason, two methods of impedance tuning are conducted.

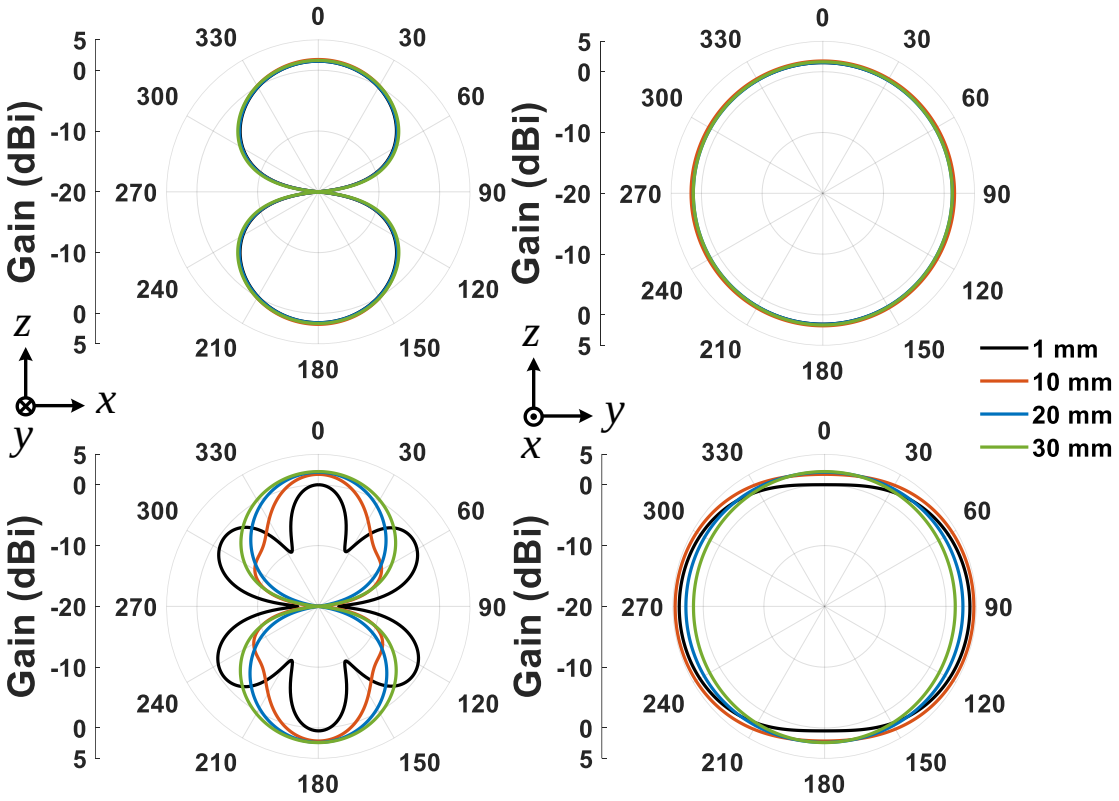

Fig. 4.3. Gain patterns of the fundamental frequency (top) and harmonic frequency (bottom) in the XZ-plane (left) and YZ-plane (right).

One of the major issues with utilizing the first frequency harmonic is that a 3λ/2 dipole has grating lobes caused by the alternating currents along its length. This method of decreasing the frequency harmonic also addresses this issue. Fig. 4.3. shows the gain patterns of the fundamental frequency (1.5 GHz) and at the harmonic frequency where S_{11} is lowest. The XZ and YZ-plane

gain patterns at the fundamental frequency show no changes as the strip width is increased. At the harmonic frequency, a change does occur. The grating lobes begin to reduce as the strip width increases. Fig. 4.4. shows the current distribution at the harmonic frequency in both a 1 mm and 30 mm thick dipole. As shown, the current in Fig. 4.4(a) has nulls along the length of the dipole creating three separate currents. This creates the three distinct lobes in Fig. 4.3. Fig. 4.4(b), however, has uniform currents across the length of the dipole. The current switches directions along the length of the feed making the null occur at the very corner of the dipole arm. With a large enough thickness, the grating lobes can be completely reduced.

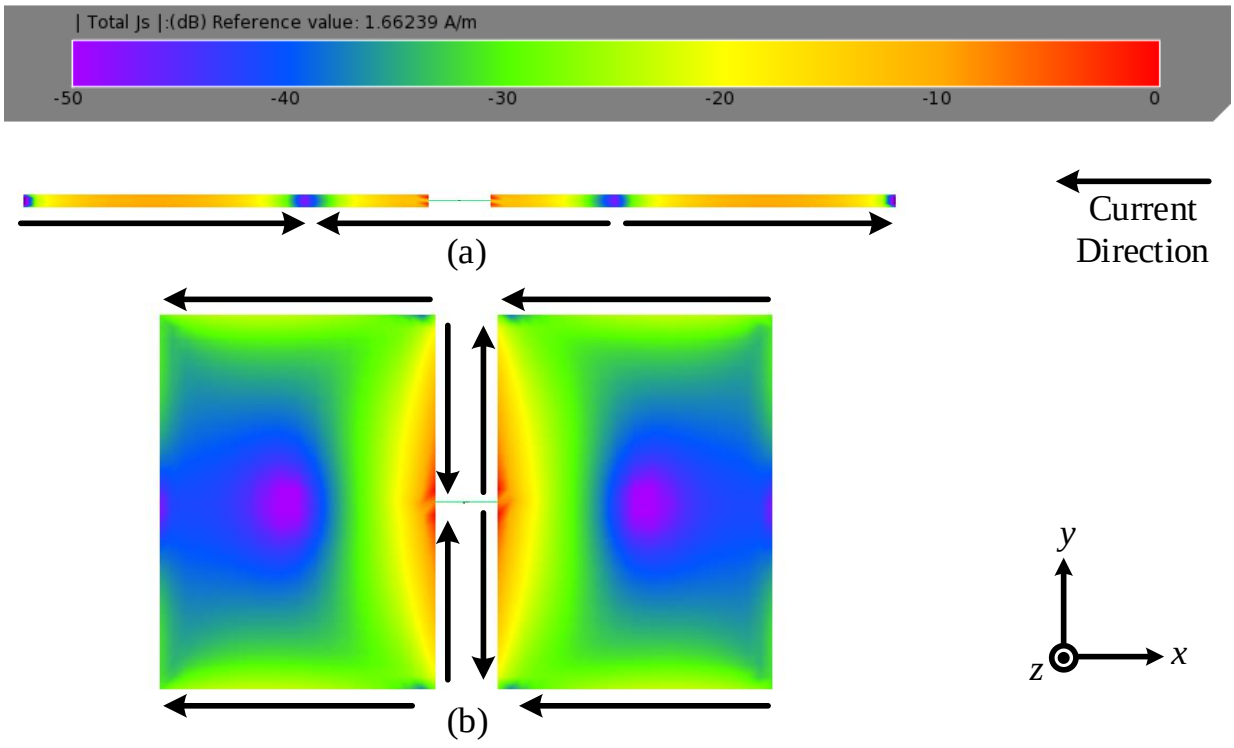

Fig. 4.4. Current density and direction of Fig. 4.1(a) with a width of 1 mm (a) and 30 mm (b).

To fix the impedance matching as the strip width is increased, the width at the edge away from the feed is investigated as shown in Fig. 4.1(b). The width of the strips near the feed is kept at 20 mm. The width away from the feed is investigated to be both shorter and longer than that of the width near the feed. Fig. 4.5. presents the results of this analysis. As the edge length increases,

the resistance is shown to increase beyond 50Ω, and the reactance varies more between the three points of 0Ω. As the edge length decreases the resistance decreases and the reactance is shown to vary less.

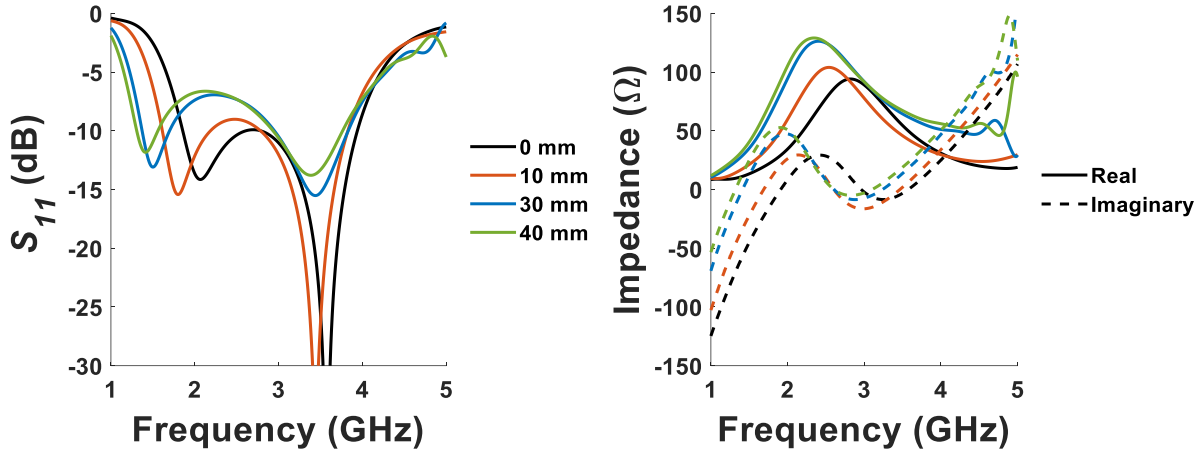

Fig. 4.5. Effect of edge length in Fig. 4.1(b) on S_{11} (left) and input impedance (right).

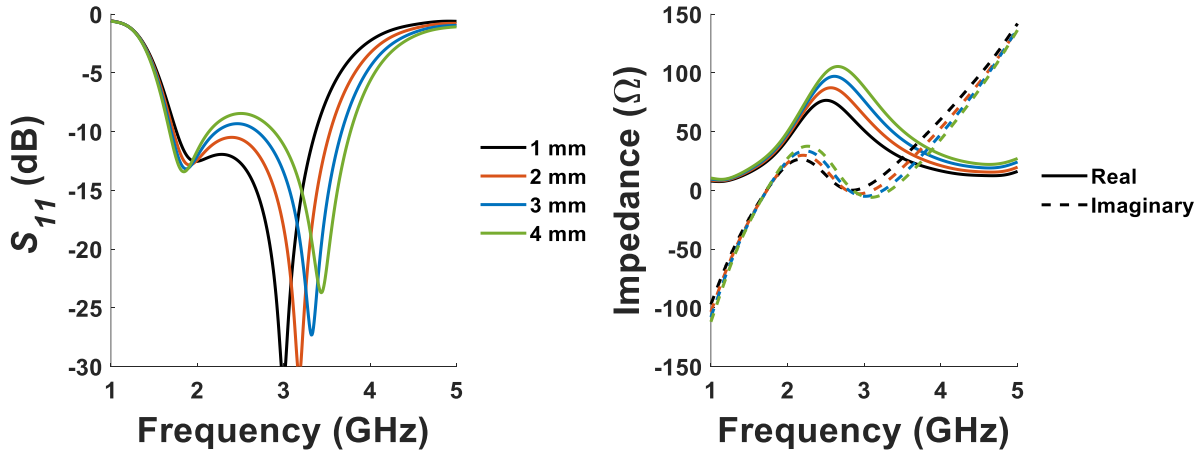

Fig. 4.6. Effect of bringing the corners together near the feed in Fig. 4.1(c) on S_{11} (left) and input impedance (right).

Another tuning method, shown in Fig. 4.1(c), is given which uses a concave-like shape near the feed. This both reduces the feed gap [45]-[46] and increases the length at the feed without increasing the width of the strip itself. With the separation at the feed kept at 5 mm, the effect of

decreasing the separation between the corners of the strip is displayed in Fig. 4.6. As this distance is decreased, the resistance is shown to decrease as well. The reactance also begins to vary less, however, the three frequencies at 0Ω begin to approach each other more which degrades the wideband properties.

Fig. 4.1(d) cuts a circle into the antenna to decrease its size and fit within a specific *kr* sphere where *k* is the wavenumber and *r* is the maximum radius enclosing the antenna. Due to removing material from the antenna, the frequency is shifted higher and needs to be decreased. Fig. 4.1(e) shows a method of top loading found to not degrade the sensitive impedance of the antenna.

4.4 Results

The antenna was optimized using a particle swarm optimizer to find the best wideband results. The final design, given in Fig. 4.1(e), has the dimensions shown in Table III where λ is calculated at 1.227 GHz. The antenna has a minimum resonant frequency of 1.227 GHz, and with a maximum radius of 39.8 mm, yields a *kr* of 1.02. The antenna is fabricated using an FR-4 substrate with copper traces shown in Fig. 4.7.

TABLE III
Dimensions of Proposed Antenna

Desc.	mm	λ
a	79.5	0.3252
b	19.3	0.0789
c	34.7	0.1419
d	51.6	0.2110
e	19.3	0.0789
f	4.9	0.0200
g	2.0	0.0082

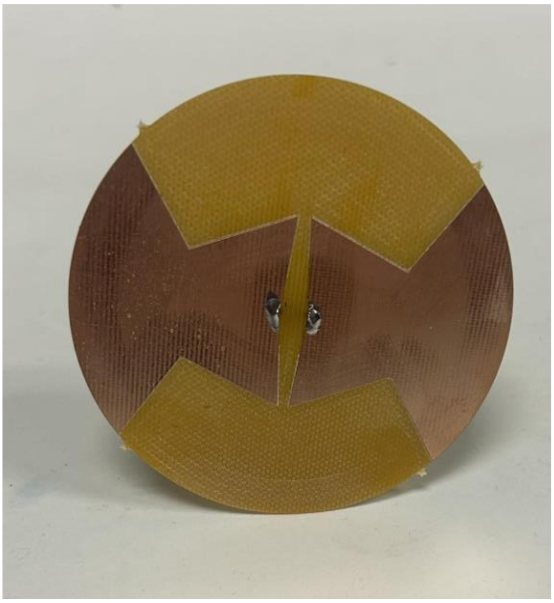

Fig. 4.7. Fabricated antenna.

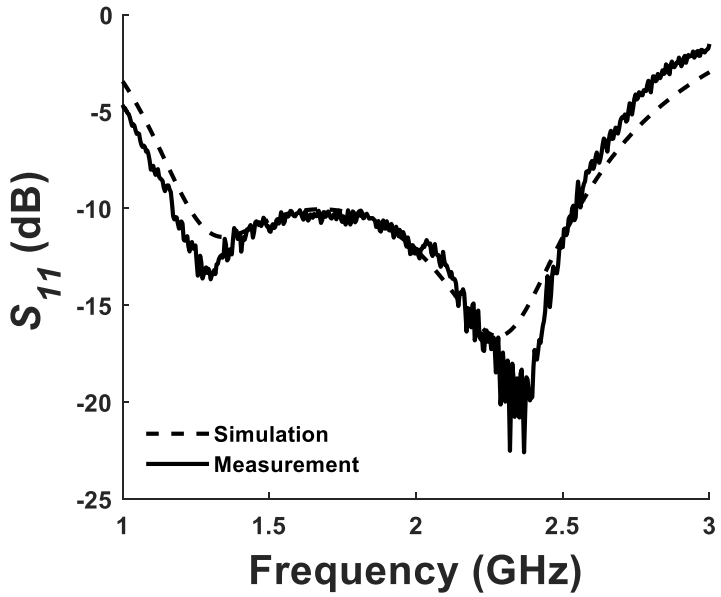

Fig. 4.8. Simulated and measured S_{11} versus frequency

Fig. 4.8. shows the simulated and measured S_{11} vs frequency. The simulated -10-dB impedance bandwidth ranges from 1.227-2.552 GHz (70.1%). The measured -10 dB impedance bandwidth ranges from 1.17-2.546 GHz (74.06%). This shows good agreement between

simulation and measurement. Fig. 4.9. shows the measured realized gain vs frequency in the zenith direction. The realized gain ranges from 1.5 to 2.6 dBi in simulation and 1.5 to 3.0 dBi in measurement across the impedance bandwidth.

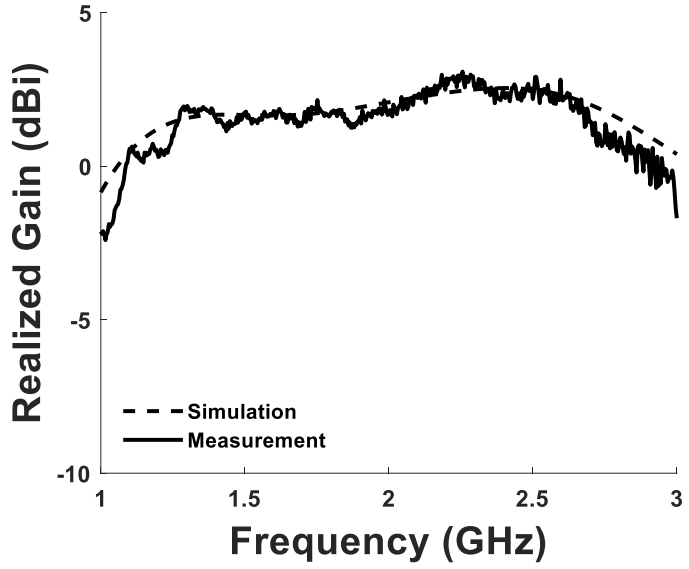

Fig. 4.9. Simulated and measured realized gain in the (+z) direction.

Fig. 4.10. gives the simulated and measured radiation patterns in the XZ and YZ-planes. The frequencies chosen are at the beginning, middle, and end of the impedance bandwidth or 1.227, 1.68, and 2.55 GHz. As expected, the patterns in the XZ-plane show no difference between the beginning and end of the impedance bandwidth with no grating lobes present. The pattern is also shown to have the characteristic dipole shape. At the highest frequency, there is slightly reduced radiation at the sides of the antenna showing a very slight directivity in the zenith direction which is expected in both the XZ and YZ-plane. The measured results are shown to have good agreement with the simulated results.

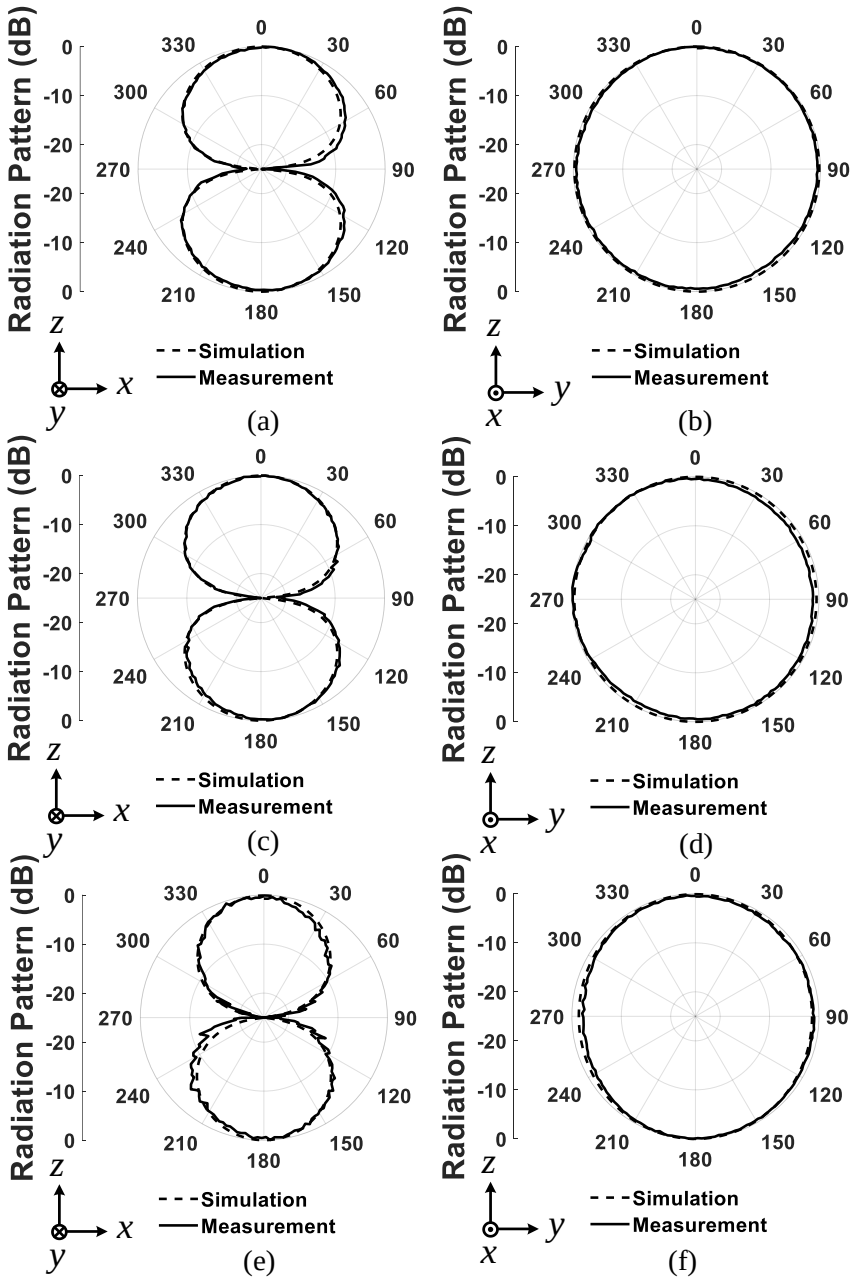

Fig. 4.10. Radiation patterns at 1.227 GHz in the XZ-plane (a) and YZ-plane (b); 1.68 GHz in the XZ-plane (c) and YZ-plane (d); and 2.55 GHz in the XZ-plane (e) and YZ-plane (f).

A comparison of other wideband dipole antennas presented in the literature are shown in Table IV. Comparing size, the proposed antenna is the second smallest with very little difference between that of [48] with a *kr* of 0.987. However, when comparing the impedance bandwidth, the

proposed antenna outshines [48] which only has an impedance bandwidth of 14.4%. Comparing impedance bandwidth, the proposed antenna has the second largest behind [23] which uses a similar tuning method. However, in comparing size the proposed antenna is much smaller than [23] with a *kr* of 1.21. When comparing the impedance bandwidth and size of the other references [24], [47], [49], the antenna presented has a smaller size and significantly larger impedance bandwidth.

TABLE IV
Comparison of Wideband Dipoles

Antenna	*kr*	Impedance bandwidth (%)	Pattern Type
[23]	1.21*	76	Omnidirectional
[24]	5.04* **	24	Directional
[47]	1.19*	47	Omnidirectional
[48]	0.987	14.4	Omnidirectional
[49]	1.46*	45.5*	Omnidirectional
Proposed	1.02	74.06	Omnidirectional

*Estimated from paper
**Contains reflector

4.5 Conclusion

A sized-reduced wideband dipole is realized using a method to decrease the frequency of the resonance that occurs at the first frequency harmonic. This is shown to reduce the grating lobes seen in the radiation pattern at the harmonic frequency. Using different tuning methods, the impedance of the antenna can be improved to create a wideband performance. The antenna is shown to maintain those wideband properties when the size is decreased. The antenna is then fabricated and measured to validate the simulation results. The measured results show good agreement with simulations.

When compared to other antennas presented in the literature, the proposed antenna shows novelty in both size and impedance bandwidth. While it comes second in size, the impedance bandwidth is nearly 60% more than the smallest antenna with a difference in *kr* of only 0.033. The

antenna also comes second in impedance bandwidth to another antenna with a much larger *kr* of 1.21 compared with 1.02. The impedance bandwidth of the other antenna is only 2% larger than the proposed. Compared to other antennas, the proposed is much smaller in *kr* and larger in impedance bandwidth showing its novelty.

CHAPTER 5

CONCLUSION

In this work, wideband antennas using dual-elements or harmonic tuning methods are analyzed through a size reduction process. The goal is to create sized-reduced antennas with enhanced impedance bandwidths and radiation characteristics to contribute to the research community. First, a comprehensive background is given on electrically small antennas, impedance bandwidth enhancing techniques, dual-element antennas, frequency harmonics in antenna propagation, and details of antenna measurements.

In Chapter 2, a comprehensive study is conducted on the spacing and size of a dual-element dipole. The analysis compares impedance bandwidth and radiation efficiency to find the best-performing antenna based on the theoretical limits defined by Wheeler and Chu. The antenna is electrically small using top loading as a size reduction technique. In size reduction, the antenna still shows the two radiation modes seen by other dual-element dipoles. It is then fabricated and measured using 18 AWG copper wire, a hybrid balun, and an anechoic chamber. The experimental results match well with the simulated results, and the antenna is compared to similar antennas in the literature showing its novelty.

In Chapter 3, an electrically small planar monopole version of the dual-element antenna is studied. The antenna is shown to have wideband properties and has the two radiation modes seen by other dual-element antennas. An analysis is done to solve issues with the radiation characteristics. Then the antenna’s size is reduced and fabricated on an FR-4 substrate. The experimental results match the simulated results. The antenna is then compared to the wire versions of the dual-element dipole and shows that it has significantly improved impedance bandwidth.

In Chapter 4, a wideband dipole is created using a tuning method to decrease the frequency of the first frequency harmonic. The tuning method is explained in detail, along with the limitation in impedance matching. Two methods are given for tuning the impedance of the antenna to achieve wideband properties. The antenna is then reduced in size, fabricated, and measured. The experimental results match well with the simulation results. The antenna is compared to others in the literature to show its novelty.

REFERENCES

[1] H. A. Wheeler, "Small antennas," *IEEE Trans. Antennas Propag.*, vol. AP-23, pp. 462-1169, July 1975.

[2] H. A. Wheeler, "Fundamental limitations of small antennas," *Proc. IRE*, vol. 35, no. 12, pp. 1479–1484, Dec. 1947.

[3] L. J. Chu, "Physical limitations of omni-directional antennas," *J. Appl. Phys.*, vol. 19, pp. 1163–1175, 1948.

[4] D. F. Sievenpiper *et al.*, "Experimental validation of performance limits and design guidelines for small antennas," *IEEE Trans. Antennas Propag.*, vol. 60, no. 1, pp. 8–19, Jan. 2012.

[5] L. P. Smith, J. C. Howell, and S. Lim, "A size-reduced, 15-element, planar Yagi antenna," *IEEE Trans. Antennas Propag.*, vol. 69, no. 4, pp. 2410–2415, Apr. 2021.

[6] G. Evans, J. Nemec, V. Obi, and S. Lim, "A low-profile, size-reduced, high gain, circularly polarized anti-jam global positioning system antenna array," *Progress In Electromagnetics Research C*, vol. 139, pp. 79–86, Jan. 2024.

[7] S. Lim and H. Ling, "Design of a closely spaced, folded Yagi antenna," *IEEE Antennas Wireless Propag. Lett.*, vol. 5, pp. 302–305, 2006.

[8] S. Lim, R. L. Rogers, and L. Hao, "A tunable electrically small antenna for ground wave transmission," *IEEE Trans. Antennas Propag*., vol. 54, pp. 417–421, 2006.

[9] J. Chen, J. Ludwig, and S. Lim, "Design of a compact log-periodic dipole array using T-shaped top loadings," *IEEE Antennas Wireless Propag. Lett.*, vol. 16, pp. 1585–1588, Jan. 2017.

[10] K. A. Leon, J. Haney, and S. Lim, “A size-reduced, circularly polarized, log-periodic dipole array,” *IEEE Antennas Wireless Propag. Lett.*, vol. 21, no. 2, pp. 371–375, Feb. 2022.

[11] Z. Hu, Z. Shen, W. Wu, and J. Lu, “Low-profile log-periodic monopole array,” *IEEE Trans. Antennas Propag.*, vol. 63, no. 12, pp. 5484–5491, Dec. 2015.

[12] C. A. Balanis, Antenna Theory: Analysis and Design, 3rd ed. New York: Wiley, 2005.

[13] R.S. Elliott, Antenna theory and design, Prentice Hall, New Jersey, 1981.

[14] Y. He, W. He and H. Wong, “A wideband circularly polarized cross-dipole antenna,” *IEEE Antennas Wireless Propag. Lett.*, vol. 13, pp. 67-70, 2014.

[15] Jeong Il Kim, Byung Moo Lee and Young Joong Yoon, “Wideband printed dipole antenna for multiple wireless services,” in Proceedings RAWCON 2001. 2001 IEEE Radio and Wireless Conference (Cat.No.01EX514), Waltham, MA, USA, 2001, pp. 153-156.

[16] B. G. Duffley, G. A. Morin, M. Mikavica and Y. M. M. Antar, “A wide-band printed double-sided dipole array,” *IEEE Trans. Antennas Propag.*, vol. 52, no. 2, pp. 628-631, Feb. 2004.

[17] K. Anim and Y. Jung, “Shortened log-periodic dipole antenna using printed dual-band dipole elements,” *IEEE Trans. Antennas Propag*. vol. 66, no. 12, pp. 6762-6771, Dec. 2018.

[18] S. Nikolaou and M. A. Abbasi, “Design and development of a compact UWB monopole antenna with easily-controllable return loss,” *IEEE Trans. Antennas Propag.*, vol. 65, no. 4, pp. 2063–2067, Apr. 2017.

[19] L. Liu, S. W. Cheung, and T. I. Yuk, “Compact MIMO antenna for portable devices in UWB applications,” *IEEE Trans. Antennas Propag.*, vol. 61, no. 8, pp. 4257–4264, Aug. 2013.

[20] G. Evans and S. Lim, “Spacing analysis of a dual-element dipole,” 2022 IEEE International Symposium on Antennas and Propagation and USNC-URSI Radio Science Meeting (AP-S/URSI), Denver, CO, USA, 2022, pp. 2056-2057.

[21] Evans, Grant J., "Analysis of Dual-Element Antenna Configurations" (2023). *Electronic Theses and Dissertations*. 2539. https://digitalcommons.georgiasouthern.edu/etd/2539

[22] J. Nemec and S. Lim, “A size-reduced dual-element dipole,” SoutheastCon 2024, Atlanta, GA, USA, 2024, pp. 872-873.

[23] R. P. Ghosh and B. Gupta, “Broadband printed dipole antennas,” 2022 IEEE International IOT, Electronics and Mechatronics Conference (IEMTRONICS), Toronto, ON, Canada, 2022, pp. 1-8.

[24] H. Huang, X. Li, and Y. Liu, “A wideband directional antenna based on hybrid mode dipole,” *IEEE Trans. Antennas Propag.*, vol. 71, no. 9, pp. 7615–7619, Sep. 2023.

[25] Y.-C. Chen, S.-Y. Chen, and P. Hsu, “Modification of radiation patterns of first harmonic mode of slot dipole for dual-frequency operation,” *IEEE Trans. Antennas Propag.*, vol. 59, no. 7, pp. 2707–2710, Jul. 2011.

[26] S.-W. Chen, D.-Y. Wang, and W.-H. Tu, “Dual-band/tri-band/broadband CPW-fed stepped-impedance slot dipole antennas,” *IEEE Trans. Antennas Propag.*, vol. 62, no. 1, pp. 485–490, Jan. 2014.

[27] P. Hirsch, A. R. Weily and P. de Souza, “Compact dual-band parasitic dipole antenna for harmonic transponders,” 2015 International Symposium on Antennas and Propagation (ISAP), Hobart, TAS, Australia, 2015, pp. 1-3.

[28] Krytar model 4005070, Frequency band: 0.5 GHz ~ 7 GHz 180° hybrid coupler, 2009. [Online]. Available at: krytar.com/pdf/4005070.pdf

[29] Q. Lin, M. -C. Tang, M. Li, Y. Duan, Z. Zhang and R. W. Ziolkowski, “IBW-enhanced, electrically small, planar, endfire-radiating huygens dipole antenna,” *IEEE Antennas Wireless Propag. Lett.*, vol. 23, no. 2, pp. 703-707, Feb. 2024.

[30] S. -H. Lee, G. Shin, S. M. Radha, J. -Y. Choi and I. -J. Yoon, “Low-profile, electrically small planar huygens source antenna with an endfire radiation characteristic,” *IEEE Antennas Wireless Propag. Lett*., vol. 18, no. 3, pp. 412-416, March 2019.

[31] Z. Wu, M. -C. Tang and R. W. Ziolkowski, “Broadside radiating, low-profile, electrically small, huygens dipole filtenna,” *IEEE Antennas Wireless Propag. Lett*., vol. 21, no. 3, pp. 556-560, March 2022.

[32] X. Chen, M. -C. Tang, D. Yi and R. W. Ziolkowski, “Wideband, electrically small, near-field resonant parasitic dipole antenna with stable radiation performance,” *IEEE Antennas Wireless Propag. Lett.*, vol. 19, no. 5, pp. 826-830, May 2020.

[33] M. -C. Tang, B. Zhou, Y. Duan, X. Chen and R. W. Ziolkowski, “pattern-reconfigurable, flexible, wideband, directive, electrically small near-field resonant parasitic antenna,” *IEEE Trans. Antennas Propag.*, vol. 66, no. 5, pp. 2271-2280, May 2018.

[34] T. Shi, Y. Wen, H. B. Wang, M. -C. Tang and X. Yuan, “Low-profile, pattern-reconfigurable, electrically small antenna based on equivalent even and odd modes,” *IEEE Antennas Wireless Propag. Lett.*, vol. 23, no. 1, pp. 304-308, Jan. 2024.

[35] J. Liang, C. C. Chiau, X. Chen, and C. G. Parini, “Study of a printed circular disc monopole antenna for UWB Systems,” *IEEE Trans. Antennas Propag.*, vol. 53, no. 11, pp. 3500–3504, Nov. 2005.

[36] A. Foudazi, H. R. Hassani, and S. Mohammad ali nezhad, “Small UWB planar monopole antenna with added GPS/GSM/WLAN bands,” *IEEE Trans. Antennas Propag.*, vol. 60, no. 6, pp. 2987–2992, Jun. 2012.

[37] H. Saghlatoon, T. Bjorninen, L. Sydanheimo, M. M. Tentzeris, and L. Ukkonen, “Inkjet-printed wideband planar monopole antenna on cardboard for RF energy-harvesting applications,” *IEEE Antennas Wireless Propag. Lett.*, vol. 14, pp. 325–328, Oct. 2015.

[38] Y. Lu, Y. Huang, H. T. Chattha, and P. Cao, “Reducing ground-plane effects on UWB monopole antennas,” *IEEE Antennas Wireless Propag. Lett.*, vol. 10, pp. 147–150, Feb. 2011.

[39] T. Aboufoul, A. Alomainy, and C. Parini, “Reconfiguring UWB monopole antenna for cognitive radio applications using gaas fet switches,” *IEEE Antennas Wireless Propag. Lett.*, vol. 11, pp. 392–394, Apr. 2012.

[40] N. Kaneda, W. R. Deal, Yongxi Qian, R. Waterhouse, and T. Itoh, “A broadband planar quasi-yagi antenna,” *IEEE Trans. Antennas Propag.*, vol. 50, no. 8, pp. 1158–1160, Aug. 2002.

[41] J. S. Herd and M. D. Conway, “The evolution to modern phased array architectures,” *Proc. IEEE*, vol. 104, no. 3, pp. 519–529, Mar. 2016.

[42] W. An *et al.*, “Low-profile wideband slot-loaded patch antenna with multiresonant modes,” *IEEE Antennas Wireless Propag. Lett.*, vol. 17, no. 7, pp. 1309–1313, Jul. 2018.

[43] A. T. Mobashsher and A. M. Abbosh, “Performance of directional and omnidirectional antennas in wideband head imaging,” *IEEE Antennas Wireless Propag. Lett.*, vol. 15, pp. 1618–1621, Jan. 2016.

[44] S.-G. Zhou and J.-Y. Li, “Low-profile and wideband antenna,” *IEEE Antennas Wireless Propag. Lett.*, vol. 10, pp. 373–376, Apr. 2011.

[45] M. D. Estarki and R. G. Vaughan, “Theoretical methods for the impedance and impedance bandwidth of the thin dipole,” *IEEE Antennas and Propagation Magazine*, vol. 55, no. 1, pp. 62–81, Feb. 2013.

[46] P. Wang, M. C. Converse, J. G. Webster, and D. M. Mahvi, “‘Improved’ calculation of reflection coefficient for coaxial antennas with feed gap effect,” *IEEE Trans. Antennas Propag.*, vol. 57, no. 2, pp. 559–563, Feb. 2009.

[47] W. S. Yeoh, K. L. Wong, and W. S. Rowe, “Wideband miniaturized half bowtie printed dipole antenna with integrated balun for wireless applications,” *IEEE Trans. Antennas Propag.*, vol. 59, no. 1, pp. 339–342, Jan. 2011.

[48] X. Chen, M.-C. Tang, D. Yi, and R. W. Ziolkowski, “Wideband, electrically small, near-field resonant parasitic dipole antenna with stable radiation performance,” *IEEE Antennas Wireless Propag. Lett.*, vol. 19, no. 5, pp. 826–830, May 2020.

[49] H. Huang, B. Li, X. Li, and Y. Liu, “A wideband dipole based on odd and even mode fusion,” *IEEE Antennas Wireless Propag. Lett.*, vol. 23, no. 2, pp. 783–787, Feb. 2024.